

# The Optical Signatures of Stochastic Processes in Many-Body Exciton Scattering

**Hao Li,<sup>1</sup> S. A. Shah,<sup>1</sup> Ajay Ram Srimath Kandada<sup>2</sup>,  
Carlos Silva,<sup>3,4,5</sup> Andrei Piryatinski,<sup>6</sup> Eric R. Bittner<sup>1</sup>**

<sup>1</sup> Department of Chemistry, University of Houston, Houston, Texas 77204, United States

<sup>2</sup> Department of Physics and Center for Functional Materials, Wake Forest University, 1834 Wake Forest Road, Winston-Salem, North Carolina 27109, United States

<sup>3</sup> School of Chemistry and Biochemistry, Georgia Institute of Technology, 901 Atlantic Drive, Atlanta, GA 30332, United States

<sup>4</sup> School of Physics, Georgia Institute of Technology, 837 State Street, Atlanta, GA 30332, United States

<sup>5</sup> School of Materials Science and Engineering, Georgia Institute of Technology, North Avenue, Atlanta, GA 30332, United States

<sup>6</sup> Theoretical Division, Los Alamos National Laboratory, Los Alamos, NM, 87545 United States

Xxxx. Xxx. Xxx. Yyyy. Aa:1–33

[https://doi.org/10.1146/\(\(please add article doi\)\)](https://doi.org/10.1146/((please add article doi)))

Copyright © Yyyy by Annual Reviews.  
All rights reserved

## Keywords

excitation-induced dephasing, many-body effects in quantum dynamics, coherent non-linear spectroscopy, quantum stochastic calculus

## Abstract

We review our recent quantum stochastic model for spectroscopic lineshapes in the presence of a co-evolving and non-stationary background population of excitations. Starting from a field theory description for interacting bosonic excitons, we derive a reduced model whereby optical excitons are coupled to an incoherent background via scattering as mediated by their screened Coulomb coupling. The Heisenberg equations of motion for the optical excitons are then driven by an auxiliary stochastic population variable, which we take to be the solution of an Ornstein–Uhlenbeck process. Here we discuss an overview of the theoretical techniques we have developed as applied to predicting coherent non-linear spectroscopic signals. We show how direct (Coulomb) and exchange coupling to the bath give rise to distinct spectral signatures and discuss mathematical limits on inverting spectral signatures to extract the background density of states.

## Contents

1. INTRODUCTION .....	3
2. NONLINEAR SPECTROSCOPIC SIGNATURES OF EID .....	5
3. NONLINEAR COHERENT SPECTROSCOPY OF NONSTATIONARY SYSTEMS .....	12
3.1. Optical Bloch Equations .....	12
3.2. Stochastic Many-body Processes .....	13
3.3. Exciton scattering contributions in the mean-field (Hartree) limit and quantum Langevin equations. ....	14
3.4. Predictions from the stochastic model .....	18
3.5. Exciton/polaron formation dynamics due to exchange interactions .....	23
4. Perspective .....	29

## 1. INTRODUCTION

It is well recognized that many-body phenomena have a profound effect on the linear and non-linear optical lineshapes of semiconductors with reduced dimensionality, in which Coulomb correlations can be particularly strong due to decreased screening and quantum confinement effects. One such effect is biexciton formation, in which Coulomb binding of two electron-hole pairs results in new two-electron, two-hole quasiparticles (1–11). Another important process that is highly relevant in exciton quantum dynamics is excitation induced dephasing (EID) (12–28), primarily investigated in two-dimensional (2D) systems such as III-V quantum wells (13, 18–20, 22–24), single-layer transition-metal dichalcogenides (25, 26), quantum dot photocells (28), and two-dimensional metal-halide perovskite derivatives (27). This can be described as the incoherent Coulomb elastic scattering between multiple excitons or between excitons and an electron-hole plasma generated with the excitation optical field. The scattering process gives rise to faster dephasing dynamics compared to the low-density pure-dephasing limit, and may be the dominant dephasing pathway at sufficiently high densities. In many systems, especially those with strong exciton-phonon coupling, the background excitations are transient and co-evolve with optical modes of the system and consequently a strictly incoherent kinetic description such as this mesoscopic approach or a kinetic Markovian Boltzmann-like scattering theory (15) cannot describe coherence dynamics. EID can be effectively rationalized from a mesoscopic perspective by means of the optical Bloch equations, which capture the effect of many-body exciton scattering on both population and coherence dynamics derived from coherent spectroscopy of semiconductors (20, 21).

---

**EID:** Excitation induced dephasing

**EIS:** Excitation induced shift

---

Recent advances towards a more microscopic perspective has been presented by Katsch et al., in which excitonic Heisenberg equations of motion are used to describe linear excitation line broadening in two-dimensional transition-metal dichalcogenides (29). Their results indicate exciton-exciton scattering from a dark background as a dominant mechanism in the power-dependent broadening EID and sideband formation. Similar theoretical modelling on this class of materials and their van der Waals bilayers have yielded insight into the role of effective mass asymmetry on EID processes (30). These modelling works highlight the need for microscopic approaches to understand nonlinear quantum dynamics of complex 2D semiconductors, but the computational expense could become considerable if other many-body details such as polaronic effects are to be included (31). As an alternative general approach, we recently developed an analytical theory of dephasing in the same vein as Anderson-Kubo lineshape theory (32, 33), but that includes *transient* EID and Coulomb screening effects, would be valuable to extract microscopic detail on screened exciton-exciton scattering from time-dependent nonlinear coherent ultrafast spectroscopy, via direct and unambiguous measurement of the homogeneous excitation linewidth (34, 35).

Here we present an overview of our work that employs a quantum stochastic approach, derived from a first-principles many-body theory of interacting excitons, to develop a mostly analytical model that describes linear and nonlinear spectral lineshapes that result from exciton-exciton scattering processes, and, importantly, their dependence on population time due to the evolution of a non-stationary/non-equilibrium excitation background (see Fig. 1(a)). Our approach is similar in spirit to the celebrated Anderson-Kubo theory (32, 33) and reduces to that in the limit of a stationary background population at sufficiently long times (36, 36). The model captures a microscopic picture of EID by integrating over the interactions of excitons produced via a well-defined coherent pathway (Fig. 10 below). The background excitons that do not have a well-defined phase relationship induced by the optical field and can be treated as a non-stationary source of quantum noise. In doing so, we can directly insert the spectral density of the bath into non-linear spectral response functions and obtain fully analytical expressions for the coherent exciton lineshapes.

We implement the model to investigate the evolution of the two-dimensional coherent excitation

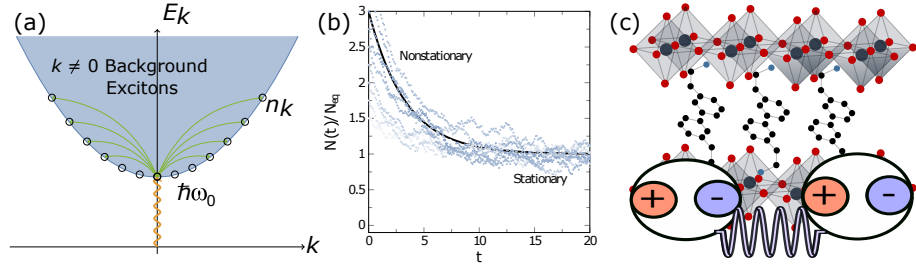


**Figure 1**

(a) Schematic representation of optical absorption of excitons and exciton-exciton scattering with a background population, where the dispersion relation is in the exciton representation and  $\vec{k} = \vec{k}_e + \vec{k}_h$  is the exciton wavevector. (b) Time evolution of population  $N(t)/N_{eq}$  from an initial nonstationary state produced by exciton injection. Individual trajectories are represented by blue dots. Asymptotically, the function reaches a stationary state that yields the Anderson-Kubo limit. (c) Crystal structure of (PEA)<sub>2</sub>PbI<sub>4</sub> with schematic representation of exciton-exciton elastic scattering interactions. Reproduced with permission from ref. 41. Copyright 2020 American Institute of Physics.

lineshape in a polycrystalline thin film of a prototypical two-dimensional single-layer metal-halide perovskite derivative, phenylethylammonium lead iodide [(PEA)<sub>2</sub>PbI<sub>4</sub>] (see Fig. 1(c) for the crystal structure). We have selected this material as a model system because of its well-defined exciton lineshape that we have modeled quantitatively within a Wannier-Mott framework (37) and because it displays strong many-body phenomena — strongly bound biexcitons at room temperature (38), and robust EID effects (27). Furthermore, we have concluded that the primary excitations are exciton polarons (31, 39) — quasiparticles with Coulomb correlations that are renormalized by lattice dynamics via polaronic effects; both electron-hole and photocarrier-lattice correlations are ingredients of the system Hamiltonian such that the lattice dressing constitutes an integral component of its eigenstates and eigenvalues. This renders the system in a highly dynamically disordered state such that lattice screening effects play an important role in shaping the lineshape (27) and in dictating nonadiabatic dynamics (40). We measure the dephasing dynamics via the homogeneous linewidth extracted by means of two-dimensional coherent excitation spectroscopy (34, 35). In our measurements, excitons generated coherently by a sequence of time-ordered and phase-matched femtosecond pulses scatter from incoherent background excitons and thereby undergo EID, which is perceived via changes of the homogeneous linewidth. We find that EID affects the complex lineshape by mixing absorptive and dispersive features in the real and imaginary spectral components; the real component of the two-dimensional coherent spectrum initially displays a dispersive lineshape that evolves into an absorptive over the timescale in which EID couplings persist, and the imaginary component evolves in the converse fashion. Furthermore, we find that the homogeneous contribution to the spectral linewidth narrows with population time, indicating a dynamic slowing down of the dephasing rate as the EID correlations active at early time dissipate. We find that the dynamic line narrowing phenomenon is reproduced by our stochastic scattering theory, which allows us to explore the effect of dynamic Coulomb screening on EID quantum dynamics.



## 2. NONLINEAR SPECTROSCOPIC SIGNATURES OF EID

Two-dimensional coherent electronic spectroscopies are very powerful techniques to identify and quantify many-body effects in semiconductors, and have been instrumental in the study EID of excitons in 2D materials (21–24, 27, 41, 42). Much of the early work was carried out by the group of Cundiff on semiconductor nanostructures (21–24), but here we focus on our recent work a Ruddlesden-Popper metal halide, namely on  $(\text{PEA})_2\text{PbI}_4$  (27, 41, 42), (PEA = phenylethylamine), which is a 2D analogue of a lead-iodide perovskite structure (see Fig. 1(c)). We highlight the peculiar signatures of EID on the 2D exciton complex lineshape, the effect of exciton density on the homogeneous linewidth, and finally on the time evolution of the spectral lineshape.

We start this review by considering the complex 2D coherent excitation spectrum of  $(\text{PEA})_2\text{PbI}_4$  to quantify the consequences of EID in the nonlinear lineshape. The linear absorption spectrum (Fig. 2(a)) reveals a family of exciton polarons with binding-energy offsets of  $\sim 40$  meV (31, 37, 39);

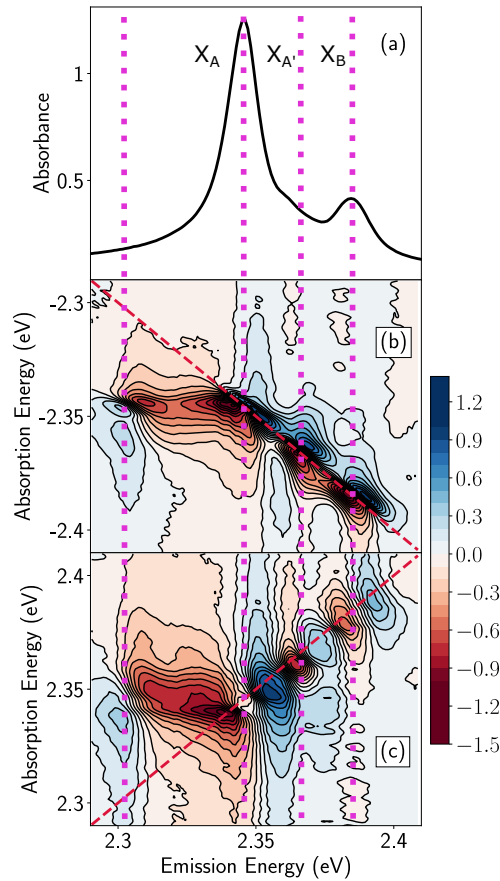


**Figure 2**

(a) Linear absorption spectrum of  $(\text{PEA})_2\text{PbI}_4$  at 5 K. Real part of the corresponding rephasing (b) and non-rephasing (c) spectra at a population time of  $\tau_p = 0$  fs and at 5 K. The bar to the right of the figure displays the vertical false color scale in arbitrary units. Reproduced with permission from ref. 41. Copyright 2020 American Institute of Physics.

**Rephasing vs. Nonrephasing:**  
Photon momentum conservation requires the output signal wave vector,  $k_s$ , be the sum of the input wave vectors. These can be understood by inspection of Fig.10. (c.f.(44))

**Rephasing:**  
 $\vec{k}_s = -\vec{k}_1 + \vec{k}_2 + \vec{k}_3$

**Non-rephasing:**  
 $\vec{k}_s = \vec{k}_1 - \vec{k}_2 + \vec{k}_3$

$\tau_p$ : Time between pulses 2 and 3 in which system is in a density-matrix population state:  $|n\rangle\langle n|$ .

we label the dominant excitons as  $X_A$  and  $X_B$ , and a shoulder at the blue edge of  $X_A$  as  $X_{A'}$ . Shown in Figs. 2(b) and 2(c) are the real parts of two different coherent excitation pathways; the time-ordering of the three optical pulses in the experiment and phase-matching conditions define the specific excitation pathways, based on which *rephasing* [Fig. 2(b)] and *non-rephasing* [Fig. 2(c)] spectra are obtained (43). In the rephasing experiment, the pulse sequence is such that the phase evolution of the polarization after the first pulse and the third pulse are of opposite sign, while in the non-rephasing experiment, they are of the same sign (see equation 52 and Fig. 10). Both measurements shown in Fig. 2 are taken at a population waiting time  $\tau_p = 0$  fs and an excitation fluence of  $40 \text{ nJ/cm}^2$ , which corresponds to an exciton density in which we have identified effects of elastic exciton-exciton scattering (27). Corresponding diagonal spectral features at the energies of  $X_A$ ,  $X_{A'}$  and  $X_B$  (indicated by the magenta vertical dotted-lines in Fig. 2) are observed, both in rephasing and non-rephasing spectra. Apart from these diagonal peaks, we observe an off-diagonal excited-state absorption feature (opposite phase with respect to the diagonal features) corresponding to a correlation between the absorption energy of  $X_A$  and emission energy  $\sim 2.3 \text{ eV}$ , which has no corresponding diagonal signal. We have assigned this cross-peak to a biexciton resonance (38).

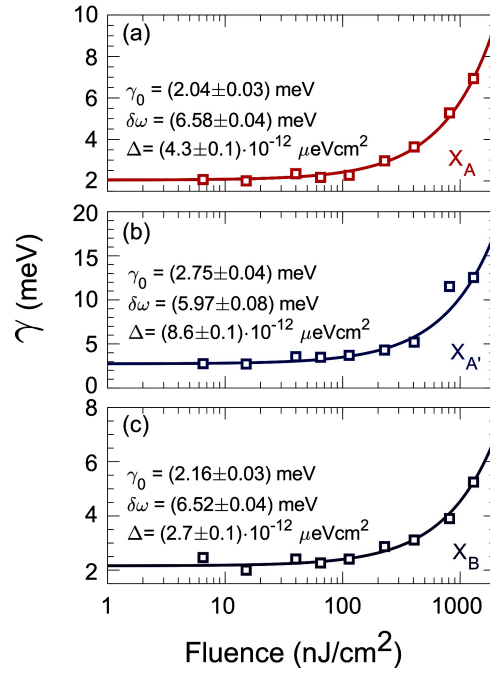


**Figure 3**

Fluence dependence of the exciton dephasing rates. Dephasing parameters  $\gamma$  of  $X_A$ ,  $X_{A'}$  and  $X_B$  are obtained from the simultaneous fitting of diagonal and anti-diagonal cuts of the norm of the zero-time rephasing spectrum, plotted as a function of excitation fluence. Squares represent the experimental linewidths and lines are the best fit to the model described in the main text. Error bars on the data are contained within the markers. The sample temperature was maintained at 5 K. Reproduced with permission from ref. 27. Copyright 2019 American Physical Society.

From the norm of the rephasing spectrum at zero time [not shown in Fig. 2 but shown below in Fig. 4(i)], one can extract the homogeneous and inhomogeneous linewidths via a global analysis of the diagonal and the anti-diagonal lineshape (34, 35). To assess the contribution of many-body

interactions on the dephasing dynamics of the different excitons, we acquired 2D coherent excitation spectra for a wide range of excitation fluences and sample temperatures (the raw data is presented in Ref. 27). The monotonic rise of  $\gamma$  with the excitation fluence at 5 K is shown in Fig. 3. Such a dependence on exciton density  $n$  is a consequence of broadening induced by exciton-exciton elastic scattering mediated by long-range Coulomb interactions:

$$\gamma_{\text{EID}}(n) = \gamma_0 + \Delta \cdot n. \quad 1.$$

Here,  $\gamma_0$  is the density-independent dephasing rate and  $\Delta$  is the exciton-exciton interaction parameter (25, 34, 35). Excitons in Ruddlesden-Popper metal halides are confined to one of the inorganic quantum wells and are electronically isolated from the others due to the large inter-layer distance (38) ( $\sim 8 \text{ \AA}$ ) imposed between them by the long organic cations. However, the sample itself, 40-nm thick, is composed of tens of these quantum wells, leading to a highly anisotropic exciton-exciton interaction. To quantify EID effects, we report the exciton-exciton interaction parameter,  $\Delta$  in units of energy per area. The associated fits and the fit parameters are displayed in Fig. 3(a), (b) and (c). While  $\gamma_0$  is approximately 2 meV with modest variation across the three probed excitonic transitions,  $\Delta$  varies more substantially. It is  $2.7 \times 10^{-12} \text{ meV cm}^2$  for  $X_B$ , increases to  $4.3 \times 10^{-12} \text{ meV cm}^2$  for  $X_A$ , and to  $8.6 \times 10^{-12} \text{ meV cm}^2$  for  $X_{A'}$ . Furthermore, for all excitons,  $\gamma$  is consistently smaller with linearly polarized excitation than with circularly polarized pulses (27). Moreover, except for exciton  $X_{A'}$ , it is independent on the helicity of the exciting pulses within our experimental uncertainty (27). When exciting the sample with linearly polarized pulses, excitons can scatter on both left and right circularly polarized excitons. However, they can only scatter with excitons of the same polarization when excited with circularly polarized pulses due to conservation of angular momentum (45).

It is not straight-forward to compare these values with those of other materials due to the ambiguities over the relevant values of the permittivity function and thus the Bohr radii. However, given the two-dimensional nature of the exciton and comparable exciton binding energies, monolayers of transition metal-dichalcogenides (TMDCs) provide a realistic benchmark. Intriguingly, previous 2D coherent excitation measurements on unencapsulated WSe<sub>2</sub> (25) and encapsulated MoSe<sub>2</sub> (26) revealed  $\Delta = 2.7 \times 10^{-12} \text{ meV cm}^2$  and  $4 \times 10^{-13} \text{ meV cm}^2$ , respectively, three and two orders of magnitude higher than the value obtained here for (PEA)<sub>2</sub>PbI<sub>4</sub>. This and the linearity of the dephasing rates over a wide range of excitation densities (45) highlights the substantial screening of the exciton-exciton interactions in these Ruddlesden-Popper metal halides. This is especially surprising given the high biexciton binding energy (38), another characteristic that (PEA)<sub>2</sub>PbI<sub>4</sub> shares with TMDC monolayers (46, 47).

We now return to the complex zero-time spectral lineshape displayed in Fig. 2. Upon close inspection, we notice that the real part of the spectrum displays dispersive shape, i.e. derivative shape about the peak energy, both for diagonal and off-diagonal resonances, in both the rephasing and non-rephasing spectrum. Note the sign-flip for the off-diagonal feature, which is consistent with its assignment to the excited state absorption to the biexcitonic state (38). Similarly, the imaginary part of the spectra (not shown in Fig. 2 but shown in Fig. 4) display an absorptive lineshape. We have demonstrated that such dispersive lineshapes are a consequence of many-body correlations (41), consistent with the analysis of similar measurements in semiconductor quantum wells (22). These lineshapes are unexpected in the absence of many-body correlations; the real part of the spectrum should be absorptive while the imaginary part dispersive. The spectra in Fig. 2 therefore reveal phase mixing due to many-body Coulomb correlations responsible for EID. In fact, Fig. 3 indicates that the EID dominates the non-linear response in the employed pump fluence range.

The evolution of the rephasing lineshape shown in Fig. 2(b) with population waiting time  $\tau_p$  is displayed in Fig. 4. The top row displays the real part of the spectrum at different values of  $\tau_p$ , the

---

**TMDC:** transition metal dichalcogenides

**Absorptive lineshape:** a diagonal slice of a 2D spectrum directly maps onto the linear absorption spectra of the system and has even reflection symmetry along the off-diagonal axis as shown in Fig. 7 for a system of J-aggregates which do not exhibit the EID effect.

**Dispersive lineshape:** the 2D spectrum has odd reflection symmetry along the off-diagonal axis, as can be seen in Fig. 6 for GaAs multiple quantum wells which show strong EID and EIS effects.

---

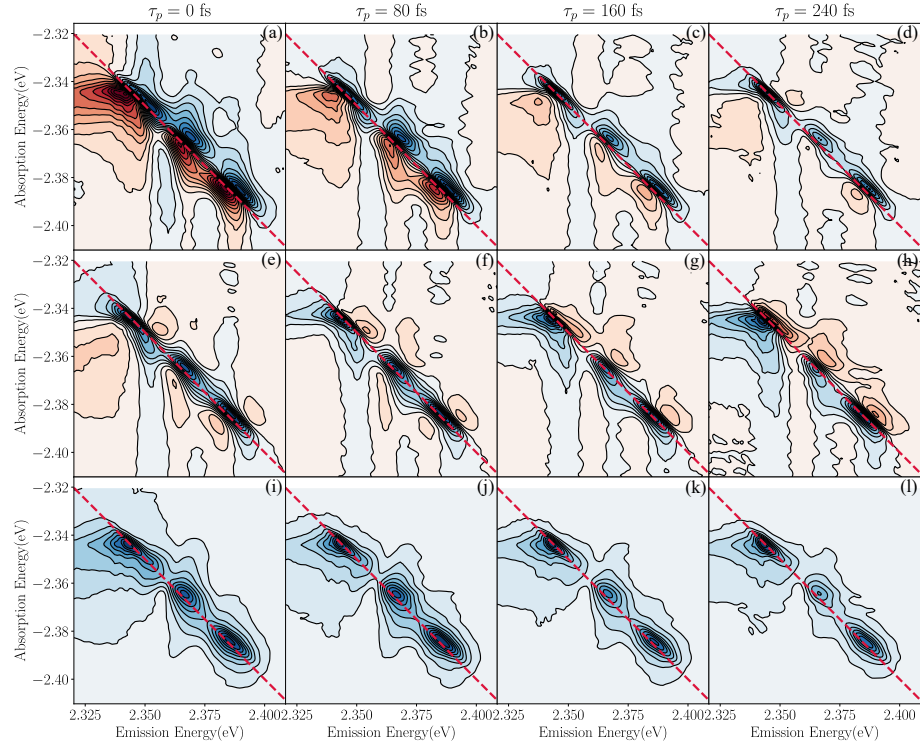


**Figure 4**

(a)–(d): Real parts of experimentally measured rephasing spectra at population times  $\tau_p$  indicated at the top of each panel, measured at 5 K. (e)–(h): Corresponding imaginary parts of the spectrum. (i)–(l): The norm (absolute value) of the optical response. All spectra components are plotted in the same relative vertical color scale to facilitate comparison of the time-dependent signal. Reproduced with permission from ref. 41. Copyright 2020 American Institute of Physics.

middle row the imaginary component, and the bottom row the norm (absolute value) of the complex spectrum. We observe that the phase scrambling phenomenon displayed in the  $\tau_p = 0$  fs spectrum [Fig. 2(b)] dissipates within  $\tau_p \leq 240$  fs: the real component of the spectrum evolves from an initially dispersive [Fig. 4(a)] to absorptive [Fig. 4(d)] lineshape, while that of the imaginary part evolves from absorptive [Fig. 4(e)] to dispersive [Fig. 4(h)] character. We note that although the evolution of the real and imaginary components of the complex lineshape is substantial over this ultrafast time window, the population decay of the diagonal features for  $X_A$  and  $X_B$  is weak, observed via the modest evolution of the total intensity in Fig. 4(i)–(l). The decay of the  $X_{A'}$  diagonal peak and the biexciton cross peak appears more substantial.

We also highlight the reduction in the total linewidth of the each diagonal exciton resonance in the absolute value of the response shown in Fig. 4(i)–(l) with population time. Inspection of these spectra reveal dynamic narrowing of  $X_A$  and  $X_B$ , primarily along the anti-diagonal spectral axis. It is more difficult to visually ascertain the linewidth evolution of  $X_{A'}$  and the biexciton cross peak given the non-negligible decay over this time period.

To quantify the measured dynamic line narrowing, we display in Fig. 5 the homogeneous linewidth as extracted as in reference 27 as a function of population time  $\tau_p$ . By this analysis, Fig. 5 shows that

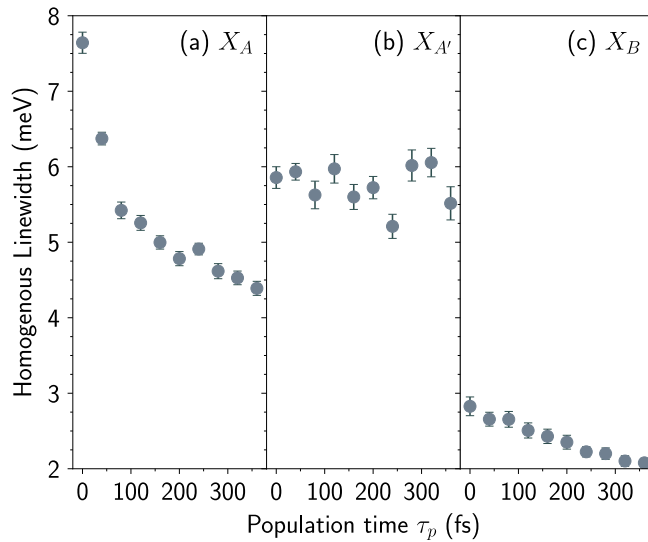


**Figure 5**

Homogenous linewidths obtained from the lineshape analysis of the absolute value of the rephasing spectra (see reference 27) plotted as a function of the population time for (a)  $X_A$ , (b)  $X_{A'}$  and (c)  $X_B$  exciton lines shown in Fig. 2(a). Reproduced with permission from ref. 41. Copyright 2020 American Institute of Physics.

the linewidth of  $X_A$  reduces most drastically, but that of  $X_B$  also reduces over a typical time window, while  $X_{A'}$  displays no line narrowing. We note that in reference 27 and in Fig. 3, we reported that  $X_A$  has a stronger density dependence of EID than  $X_B$ , which is consistent with the observation derived from Figs. 5(a) and 5(c). We have found  $X_B$  to be more strongly displaced along phonon coordinates involving octahedral twist in the plane of the inorganic layer, and out of plane scissoring of the Pb—I—Pb apex (39). The stronger exciton-phonon coupling implies that  $X_B$  is more susceptible to dynamic screening than  $X_A$ , which is consistent with the data in Fig. 5 and Fig. 3. Finally, we point out that the asymptotic value of the homogeneous linewidth for  $X_A$ ,  $X_{A'}$ , and  $X_B$  tends towards the low-exciton-density linewidths that we reported in reference 27.

The linewidth of  $X_{A'}$  remains relatively constant over the probed population time. While this might initially suggest that this resonance is immune to EID effects, we note that the real part of the rephasing spectrum associated to this particular transition exhibits a dispersive lineshape at all population times, consistent with the initial lineshapes of  $X_A$  and  $X_B$ . This indicates the clear presence of EID effects, as also confirmed by the density dependent linewidth previously published in Ref 27. The trend shown in Fig 5(b), on the other hand, suggests that the inter-exciton scattering does not evolve with the population time, at least within the probed time range. Inspection of the the lineshape, however, suggests that the dispersive shape of the real part is preserved at all population times, suggesting  $X_{A'}$  is subjected to EID over a much longer period of time than the other two resonances. Following the arguments developed by the theoretical work described below in the review, this implies the presence of a background exciton population that contributes to the scattering of  $X_{A'}$  and whose stochastic evolution is that of the background of the other two resonances. This reiterates our assignment of the multiple resonances within the spectral structure to excitonic states of distinct character and possibly specific origin (31).

The early-time complex lineshape indicative of EID many-body correlations, shown in Figs. 2 and

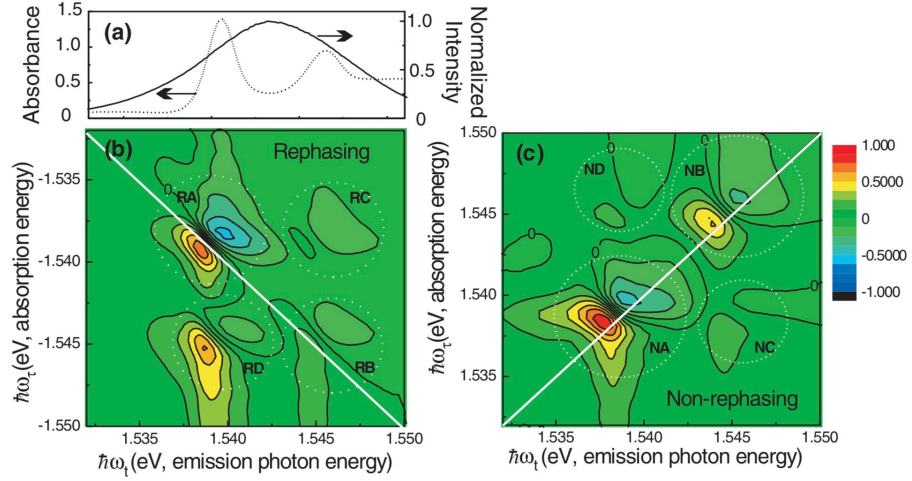


**Figure 6**

Linear absorption, excitation pulse spectrum (a) and experimental real spectra for the rephasing (b) and nonrephasing (c) pulse sequences. Reproduced with permission from Ref. 22.

4, have been observed previously in GaAs quantum wells (22). Fig. 6 displays the real part of the zero-population-time rephasing and non-rephasing spectra at excitation densities in which the signature of many-body interaction is clearly observed, and we identify a dispersive lineshape akin to that observed in Fig. 2 for (PEA)<sub>2</sub>PbI<sub>4</sub>. In contrast, Fig. 7 displays typical 2D spectra for a conjugated polymeric J-aggregate material (H2TPPS) taken in solution at room temperature. In this case, exciton/exciton interaction is essentially non-existent and the resulting 2D spectral maps show absorptive line-shapes in both the rephasing and non-rephasing signals. This latter case is well-described using current theoretical treatments of non-linear spectroscopy assuming that the line-shape results from stationary fluctuations about an average transition frequency.

We point out that inorganic and hybrid inorganic-organic semiconductors, such as GaAs quantum wells and (PEA)<sub>2</sub>PbI<sub>4</sub> discussed in this section, Coulomb exciton-exciton interactions are strong and EID effects are evident in the 2D coherent spectral lineshape. Organic semiconductors display a contrasting situation, exemplified by measurements of 2D coherent spectra in molecular J aggregates (Fig. 7) (48). In this work, many-body excitonic effects are identified and analyzed, but the distinct lineshape effects in Figs. 2, 4, and 6 are not observed. This points to the highly localized nature of excitons in organic systems, where interactions with local vibration are dominant.

In the next section, we present an overview of our recent work in developing spectroscopic models in which the energy gaps evolve in concert with a bath of background excitations that are both non-equilibrium and non-stationary as the result of being incoherently pumped by a series of laser pulses. Here, we develop the theory starting from a microscopic/many-body description of a system of excitons interacting via long-range Coulomb interactions and coupled to a dissipative environment. The theory is developed by deriving stochastic Langevin equations for the excitons and then using these derive spectral responses in the mean-field limit. The resulting model reduces to the well-known Anderson-Kubo model in the limit that the excitonic dynamics are stationary. The model provides a microscopic origin for the EID and EIS effects in semiconductor systems. As part of our review, we work through many of the technical details of the theory and our use of stochastic calculus to derive

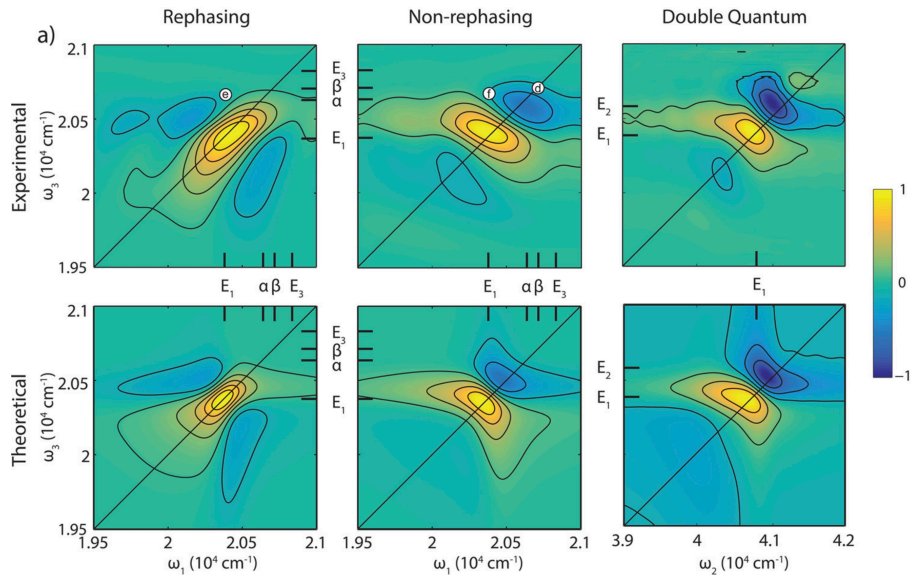


**Figure 7**

(a) Examples of experimental (upper line) and simulated (lower line) 2D maps obtained in the rephasing (R), non rephasing (NR), and double-quantum (2Q) configurations for H2TPPS aggregates in solution at room temperature. The R and NR maps report the real part of the signal at  $t_2 = 0$  fs. The 2Q maps refer to  $t_1 = 0$ . All of the maps are normalized to their maximum. The energies of relevant states and the coordinates where the traces shown in panels d–f are extracted are also pinpointed in the maps. Reproduced from Ref. 48.

analytical expressions for the spectral responses.



### 3. NONLINEAR COHERENT SPECTROSCOPY OF NONSTATIONARY SYSTEMS

#### 3.1. Optical Bloch Equations

The many-body exciton scattering signatures in the 2D coherent lineshape, reported in Fig. 6 for GaAs quantum wells, were rationalized by numerical simulation based on modified optical Bloch equations (OBE) (22). For a two-level system that includes both excitation-induced dephasing (EID) and excitation-induced shift (EIS) effects, the off-diagonal term of the density matrix,  $\rho_{12}$ , follows the following equation of motion:

$$\begin{aligned}\dot{\rho}_{12} &= -[(\gamma_0 + \gamma' N \rho_{22}) - i(\omega_0 + \omega' N \rho_{22})] \rho_{12} + \frac{i}{\hbar} \vec{\mu}_{12} \cdot \vec{E}(t) (\rho_{22} - \rho_{11}) \\ &= i[(\omega_0 + i\gamma_0) + (\omega' + i\gamma') N \rho_{22}] \rho_{12} + \frac{i}{\hbar} \vec{\mu}_{12} \cdot \vec{E}(t) (\rho_{22} - \rho_{11}),\end{aligned}\quad 2.$$

where  $\gamma_0$  is the natural dephasing rate,  $\rho_{11}$  and  $\rho_{22}$  are the ground and excited state populations connected by coherence term  $\rho_{12}$ ,  $N$  is the number density of chromophores and  $\gamma'$  and  $\omega'$  characterize the collision rate and collective interactions within the excited state population. The last term corresponds to the driving field of the laser and dipole coupling between the ground and excited states. As the OBE system evolves, the total dephasing rate,  $(\gamma_0 + \gamma' N \rho_{22}(t))$ , and the phase oscillation frequency,  $(\omega_0 + \omega' N \rho_{22}(t))$ , both depend upon the fraction of chromophores in the excited state at time  $t$ .

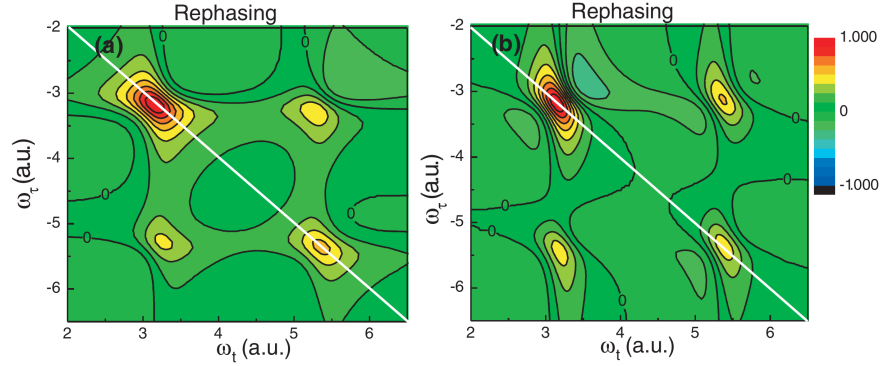


**Figure 8**

Calculated real spectra for the rephasing sequence. (a) is based on a simple V system without any many-body interactions, while excitation-induced dephasing is included in (b). Reproduced with permission from Ref. 22

Fig. 8 shows the predicted four-wave mixing signals for a two-level system with and without the term attributed to the EID component. While the simple OBE approach does capture the narrowing, shift, and asymmetry of the lineshape, it fails to capture the phase scrambling that is clearly observed in the experimental signals in Fig. 6. The OBE real signals are clearly absorptive, rather than dispersive.

However, the decomposition of a 2D spectrum into its real and imaginary parts depends on the techniques applied e.g., through the comparison to an independent spectrally resolved differential transmission measurement. In other words, the feature of dispersive lineshape may be hidden in the imaginary part of the spectrum. On the other hand, from the Green's function approach, the EID and EIS are attributed respectively to the real and imaginary parts of the exciton self-energy renormalization. Therefore, the term of  $\omega' + i\gamma'$  in Eq. 2 cannot be treated separately in a quantum mechanical theory. As we will illustrate later in our model, including the many-body interaction in the Hamiltonian



leads to the excitation-induced dephasing and frequency shift effect in the spectral signals simultaneously.

What is then desired is an approach that incorporates the many-body dynamics of a dark, non-optical population that co-evolves with the optical signals. In this section, we accomplish this via the use of a stochastic line-shape approach, taken in the limit that the non-optical population contributes non-equilibrium and non-stationary contributions to the fluctuations of the optical energy gap.

### 3.2. Stochastic Many-body Processes

Our model is initiated by assuming that at  $t = 0$  a non-stationary population of background excitations is created by a broad-band laser excitation. This physical picture is sketched in Fig. 1. In the current work, excitation occurs with a sequence of phase-matched and time-ordered femtosecond pulses used to measure a coherent nonlinear excitation spectrum, and the excitons produced and measured via a well defined coherent pathway (see Fig. 10 for the relevant ones in this work) are assumed to scatter elastically with their incoherent counterparts — excitons that are produced by the pulse sequence but have no phase relationship to those that produce signal in our experiments. The initial background population can be characterized by an average population  $N_0$  and variance  $\sigma_{N_0}^2$  both of which depend upon the excitation pulse as well as the density of states of the material. Optical excitations at  $k = 0$  evolve in concert with a non-stationary ( $k \neq 0$ ) background of excitations in which the interaction determined by a screened Coulomb potential giving rise to a noisy driving term that effectively modulates the exciton energy gap.

Here we consider the case where we have an ensemble of bosonic excitons described by a Hamiltonian written in second-quantized form as

$$H = \sum_k \hbar \omega_k a_k^\dagger a_k + \frac{1}{2} \sum_{kk'q} V_q a_{k+q}^\dagger a_{k'-q}^\dagger a_{k'} a_k, \quad 3.$$

where  $V = L^3$  is the unit volume and  $V_q$

$$V_q = \frac{1}{(2\pi)^3} \int V(\mathbf{r}) e^{-i\mathbf{q} \cdot \mathbf{r}} d\mathbf{r} \quad 4.$$

is the Fourier component of the many-body interaction potential. We now collect the  $k \neq 0$  terms by keeping those interacting with  $k = 0$  excitons and involving no more than two  $k \neq 0$  states.

$$\begin{aligned} H = & \hbar \omega_0 a_0^\dagger a_0 + \sum_{q \neq 0} \hbar \omega_q a_q^\dagger a_q + \frac{V_0}{2} a_0^\dagger a_0^\dagger a_0 a_0 \\ & + a_0^\dagger a_0 \left[ 2V_0 \sum_{q \neq 0} (a_q^\dagger a_q) \right] \\ & + a_0^\dagger a_0^\dagger \left[ \frac{V_0}{2} \sum_{q \neq 0} a_q a_{-q} \right] + a_0 a_0 \left[ \frac{V_0}{2} \sum_{q \neq 0} a_q^\dagger a_{-q}^\dagger \right] \end{aligned} \quad 5.$$

and focus only the  $k = 0$  term

$$\begin{aligned} H/\hbar = & \omega_0 a_0^\dagger a_0 + \Omega \hat{A}^\dagger \hat{A} \\ & + \frac{\gamma_1}{2} \left( a_0^\dagger a_0^\dagger a_0 a_0 + 4a_0^\dagger a_0 \hat{N} + a_0^\dagger a_0 \hat{A} \hat{A} + a_0 a_0 \hat{A}^\dagger \hat{A}^\dagger \right) \end{aligned} \quad 6.$$

where the  $\hat{A}$ ,  $\hat{A}^\dagger$ , and  $\hat{N}$  operators are collective bath operators defined by inspection of Eq. 5.  $\hbar \gamma_1 = V_0$  is the exciton-exciton interaction, which we obtain from the  $s$ -wave scattering length  $a$  and reduced

mass  $\mu$  within the Born approximation (49)

$$\gamma_1 = \frac{4\pi\hbar a}{\mu}. \quad 7.$$

This assumption does not rely upon the specific form of the exciton-exciton interaction, only that it be of finite range. In the current context, this interaction will be due to Coulomb-mediated exciton-exciton scattering that gives rise to EID (27). However, it is possible that each distinct exciton within the family of the 2D perovskite system considered here (31) have a distinct and unique value of  $\gamma_1$ , as we reported in ref. 27, where we demonstrated distinct Coulomb screening of different exciton polarons. For purposes of our theoretical model, we assume that the system has a *single* exciton species that is susceptible to many-body scattering and therefore EID mediated via  $\gamma_1$ .

### 3.3. Exciton scattering contributions in the mean-field (Hartree) limit and quantum Langevin equations.

The term involving  $\hat{N}$  introduces mean-field between the  $k = 0$  excitons and the net population of the  $k \neq 0$  excitons. This term introduces energy fluctuation simply due to scattering of the  $k \neq 0$  population from the  $k = 0$  population. The other two terms give rise to fluctuations/dissipation due to exciton pair creation/annihilation. For the moment, we shall neglect these terms, but will return to discussing them in a later section.

We now assume that the collective operators for the background (dark) excitons

$$\gamma_1 \hat{A}^\dagger \hat{A} = \sum_{q \neq 0} (V_0 + V_q) a_q^\dagger a_q$$

are coupled to an ensemble of otherwise unspecified bath oscillators  $b_i/b_i^\dagger$  as described by an auxiliary Hamiltonian of the form:

$$\begin{aligned} H_{aux} = & \hbar\Omega \left( \hat{A}^\dagger \hat{A} + \frac{1}{2} \right) + \sum_i \hbar\omega_i \left( \hat{b}_i^\dagger \hat{b}_i + \frac{1}{2} \right) \\ & + \sum_i \left( g_i \hat{A}^\dagger \hat{b}_i + g_i^* \hat{A} \hat{b}_i^\dagger \right). \end{aligned} \quad 8.$$

For convenience we rotate the operators in the Heisenberg representation (denoted by subscript H) according to their respective frequency

$$\hat{A}(t) = \hat{A}_H(t) e^{-i\Omega t} \quad 9.$$

$$\hat{b}_i(t) = \hat{b}_{i,H}(t) e^{-i\omega_i t} \quad 10.$$

so that  $\hat{A}$  and  $\hat{b}_i$  evolve only under the influence of the interaction. Then we have the Heisenberg equation of motion for the rotated exciton operator

$$\frac{d}{dt} \hat{A}(t) = - \int_0^{t-t_0} d\tau \kappa(\tau) \hat{A}(t-\tau) + \hat{F}(t), \quad 11.$$

where

$$\kappa(\tau) = \frac{1}{\hbar^2} \sum_i |g_i|^2 e^{i(\Omega - \omega_i)\tau} \quad 12.$$

$$\hat{F}(t) = -\frac{i}{\hbar} \sum_i g_i \hat{b}_i(t_0) e^{i(\Omega - \omega_i)t}. \quad 13.$$

Considering that bath oscillator frequencies  $\omega_i$  cover a wide range and  $|g_i|^2$  may vary slowly with  $\omega_i$ , the oscillating exponentials in  $\kappa(\tau)$  interfere destructively for  $\tau > 0$  and  $\kappa(\tau)$  becomes negligible when  $\tau \gg \tau_c$ , where  $\tau_c$  is the correlation time of the bath. In addition, the time scale (damping time) of the excitons is often much greater than  $\tau_c$ , so that one may replace  $\hat{A}(t - \tau)$  by  $\hat{A}(t)$  from the integral. Eq.(11) can be rewritten as

$$\frac{d}{dt}\hat{A}(t) = -\left(\frac{\Gamma}{2} + i\Delta\right)\hat{A}(t) + \hat{F}(t), \quad 14.$$

in which

$$\Gamma = \frac{2\pi}{\hbar^2} \sum_i |g_i|^2 \delta(\Omega - \omega_i), \quad 15.$$

$$\Delta = \mathcal{P} \sum_i \frac{|g_i|^2}{\hbar^2 (\Omega - \omega_i)} \quad 16.$$

describe the spontaneous emission rate and the spontaneous radiative shift of the system operator, respectively.

The bath operator  $\hat{F}(t)$  has the following properties

$$\langle \hat{F}(t) \rangle = \text{Tr} [\sigma_A \sigma_B \hat{F}(t)] = 0, \quad 17.$$

$$\langle \hat{F}(t') \hat{F}(t) \rangle = \langle \hat{F}^\dagger(t') \hat{F}^\dagger(t) \rangle = 0, \quad 18.$$

$$\langle \hat{F}^\dagger(t') \hat{F}(t) \rangle = \sum_i \frac{1}{\hbar^2} |g_i|^2 \langle n_i \rangle e^{i(\Omega - \omega_i)(t - t')}, \quad 19.$$

$$\langle \hat{F}(t') \hat{F}^\dagger(t) \rangle = \sum_i \frac{1}{\hbar^2} |g_i|^2 (\langle n_i \rangle + 1) e^{i(\Omega - \omega_i)(t - t')}, \quad 20.$$

where  $n_i = b_i^\dagger(t_0) b_i(t_0)$ . Therefore  $\hat{F}(t)$  can be considered as a Langevin force fluctuating around its zero average value, and Eq.(14) is a Langevin equation. The diffusion coefficients are defined as

$$2D_N = \int_{-\infty}^{+\infty} d\tau \langle \hat{F}^\dagger(t - \tau) \hat{F}(t) \rangle \quad 21.$$

$$2D_A = \int_{-\infty}^{+\infty} d\tau \langle \hat{F}(t) \hat{F}^\dagger(t - \tau) \rangle, \quad 22.$$

with subscripts  $N$  and  $A$  denote for the normal and anti-normal order of  $\hat{F}^\dagger$  and  $\hat{F}$ . Furthermore,

$$2D_N = \Gamma' = \Gamma \langle n(\Omega) \rangle \quad 23.$$

$$2D_A = \Gamma' + \Gamma = \Gamma (1 + \langle n(\Omega) \rangle), \quad 24.$$

where  $\langle n(\Omega) \rangle$  is the average number of quanta of the bath modes having the same frequency  $\Omega$  as the system.

In the mean-field Hamiltonian Eq.(6), the background exciton population operator  $\hat{N}(t) = \hat{A}^\dagger(t) \hat{A}(t)$  is of our interest. Using Eq.(14) we deduce the Heisenberg equation of motion

$$\frac{d}{dt} [\hat{A}^\dagger(t) \hat{A}(t)] = -[\Gamma + i(\Delta - \Delta^*)] \hat{A}^\dagger(t) \hat{A}(t) + \hat{F}^\dagger(t) \hat{A}(t) + \hat{A}^\dagger(t) \hat{F}(t). \quad 25.$$

Integrating the differential equation Eq.(14) from  $t_0$  to  $t'$

$$\hat{A}(t') = \hat{A}(t_0) e^{-(\Gamma/2 + i\Delta)(t' - t_0)} + \int_{t_0}^{t'} dt'' \hat{F}(t'') e^{-(\Gamma/2 + i\Delta)(t' - t'')}. \quad 26.$$

For  $t_0 \rightarrow -\infty$ , the first term is negligible and we have, by multiplying both sides by  $\hat{F}^\dagger(t)$ ,

$$\langle \hat{F}^\dagger(t) \hat{A}(t') \rangle = \int_{t_0}^{t'} dt'' \langle \hat{F}^\dagger(t) \hat{F}(t'') \rangle e^{-(\Gamma/2+i\Delta)(t'-t'')}. \quad 27.$$

$\hat{F}^\dagger(t)$  is only correlated with  $\hat{A}(t')$  in an interval of  $t \in (t', t' - \tau_c)$  and  $\langle \hat{F}^\dagger(t) \hat{F}(t') \rangle$  varies much more rapidly with  $t - t'$  than the exponential, therefore

$$\langle \hat{F}^\dagger(t) \hat{A}(t) \rangle \approx \int_{t_0}^t dt'' \langle \hat{F}^\dagger(t) \hat{F}(t'') \rangle \quad 28.$$

$$\langle \hat{A}^\dagger(t) \hat{F}(t) \rangle \approx \int_{t_0}^t dt'' \langle \hat{F}^\dagger(t'') \hat{F}(t) \rangle. \quad 29.$$

Let  $\tau = t - t''$ , hence we have

$$\langle \hat{F}^\dagger(t) \hat{A}(t) \rangle + \langle \hat{A}^\dagger(t) \hat{F}(t) \rangle = \int_{-(t-t_0)}^{+(t-t_0)} d\tau \langle \hat{F}^\dagger(t-\tau) \hat{F}(t) \rangle = 2D_N. \quad 30.$$

The background exciton population operator  $\hat{N}(t) = \hat{A}^\dagger(t) \hat{A}(t)$  satisfies

$$\begin{aligned} \frac{d}{dt} \langle \hat{A}^\dagger(t) \hat{A}(t) \rangle &= \left\langle \frac{d}{dt} [\hat{A}^\dagger(t)] \hat{A}(t) \right\rangle + \left\langle \hat{A}^\dagger(t) \frac{d}{dt} [\hat{A}(t)] \right\rangle \\ &= -\Gamma \langle \hat{A}^\dagger(t) \hat{A}(t) \rangle + \langle \hat{F}^\dagger(t) \hat{A}(t) \rangle + \langle \hat{A}^\dagger(t) \hat{F}(t) \rangle \\ &= -\Gamma \langle \hat{A}^\dagger(t) \hat{A}(t) \rangle + 2D_N. \end{aligned} \quad 31.$$

The nonzero average value of  $\langle \hat{F}^\dagger(t) \hat{A}(t) + \hat{A}^\dagger(t) \hat{F}(t) \rangle$  prevents us from treating it as a Langevin force. However, the equation of motion Eq.(31) can still be described by a generalized Ornstein-Uhlenbeck equation with a drift  $2D_N/\Gamma$

$$dN(t) = -\Gamma \left[ N(t) - \frac{2D_N}{\Gamma} \right] dt + \sigma dW(t), \quad 32.$$

where  $dW(t)$  represents a Wiener process. Because the background population operator  $\hat{N}(t)$  and  $k=0$  exciton operator  $a_0/a_0^\dagger$  evolves independently, hereafter we treat  $N(t) = \text{Tr}[\hat{N}(t)]$  as a function rather than an operator. The formal solution is

$$N(t) = N(0)e^{-\Gamma t} + \frac{2D_N}{\Gamma} (1 - e^{-\Gamma t}) + \sigma \int_0^t e^{-\Gamma(t-s)} dW_s. \quad 33.$$

The covariance function does not depend on the drift,

$$\text{Cov}[N(s), N(t)] = \sigma_{N_0}^2 e^{-\Gamma(s+t)} + \frac{\sigma^2}{2\Gamma} [e^{-\Gamma|t-s|} - e^{-\Gamma(t+s)}].$$

However, the average value of the stationary state no longer vanishes but is determined by the drift

$$\langle N(t) \rangle_{ss} = \lim_{t \rightarrow \infty} \left[ N(0)e^{-\Gamma t} + \frac{2D_N}{\Gamma} (1 - e^{-\Gamma t}) \right] = \frac{2D_N}{\Gamma}. \quad 34.$$

The drift term can also be approximated by  $2D_N/\Gamma = \langle n(\Omega) \rangle$ , where  $\langle n(\Omega) \rangle$  is the average number of quanta of the bath modes having the same frequency  $\Omega$  as the system. This indicates the equilibrium between the system and the bath.

We can write the damping velocity as an operation denoted by  $\mathcal{D}(\hat{A}(t))$

$$\mathcal{D}(\hat{A}(t)) = -\left(\frac{\Gamma}{2} + i\Delta\right)\hat{A}(t) \quad 35.$$

$$\mathcal{D}(\hat{A}^\dagger(t)) = -\left(\frac{\Gamma}{2} - i\Delta\right)\hat{A}^\dagger(t) \quad 36.$$

$$\mathcal{D}(\hat{A}^\dagger(t)\hat{A}(t)) = -\Gamma\hat{A}^\dagger(t)\hat{A}(t) + \Gamma'. \quad 37.$$

Then we have

$$2D_N = \left\langle \mathcal{D}(\hat{A}^\dagger\hat{A}) - \mathcal{D}(\hat{A}^\dagger)\hat{A} - \hat{A}^\dagger\mathcal{D}(\hat{A}) \right\rangle = \Gamma' = \Gamma\langle n(\Omega) \rangle, \quad 38.$$

which can be considered as a generalization of the Einstein relation ( $D = Mk_B T \gamma$ ) between the diffusion coefficient  $D$  and the decay rate  $\Gamma$ .

Similarly, the diffusion coefficient  $D_A$  is related to  $\hat{A}(t)\hat{A}^\dagger(t)$  by

$$\frac{d}{dt} \langle \hat{A}(t)\hat{A}^\dagger(t) \rangle = -\Gamma \langle \hat{A}(t)\hat{A}^\dagger(t) \rangle + 2D_A. \quad 39.$$

Since  $\langle [\hat{A}(t), \hat{A}^\dagger(t)] \rangle = 1$ , we conclude

$$D_A - D_N = \frac{\Gamma}{2}. \quad 40.$$

Note that  $D_N$  and  $D_A$  are originated from the *non-Hamiltonian* part of the damping/relaxation. The radiative shift term of  $\Delta$  can be absorbed into an effective Hamiltonian thus it is not included in the equations of motion for  $A^\dagger(t)A(t)$  and  $A(t)A^\dagger(t)$ .

For a stationary background population, i.e.  $\langle N(t) \rangle = 0$  the covariance evolves according to

$$\langle N(t)N(s) \rangle = \langle N(t-s)N(0) \rangle = \frac{\sigma^2}{2\Gamma} \exp(-\Gamma|t-s|).$$

In this limit, our model reduces to the Anderson-Kubo model in which the frequency fluctuates about a stationary average according to an Ornstein-Uhlenbeck process. In this case, the population relaxation time in our model is equivalent to the correlation time in Anderson-Kubo and this gives the rate at which the environment relaxes back to its stationary average given a small push. Moreover, the fluctuation amplitude,  $\Delta\omega^2$ , in Anderson-Kubo is equivalent to  $\sigma^2/2\Gamma$  in our model. As we shall show, what appears at first to be a simple modification to the dynamics of a system has significant implications in terms of the non-linear spectral response of the system.

At time  $t = 0$ , we push the background population significantly away from the steady-state distribution to an initial value of  $\langle N(0) \rangle = N_0$ , the population evolves as

$$N(t) = N(0)e^{-\Gamma t} + \sigma \int_0^t e^{-\Gamma(t-s)} dW(s). \quad 41.$$

and

$$\langle N(t) \rangle = e^{-\Gamma t} N_0, \quad 42.$$

where  $N_0$  is the mean number of background excitations present at time  $t = 0$ .

In principle, there will be a distribution about this mean characterized by a variance  $\sigma_{N_0}^2$ . As a result, we break reversibility and the time symmetry of the correlation functions. Mathematically, this means that  $\langle N(t)N(s) \rangle \neq \langle N(t-s)N(0) \rangle$  since the choice of initial time is no longer arbitrary.

---

#### Itô lemma:

$(dW(t))^2 = dt$  where  $W(t)$  is the Wiener process.

#### Normal calculus:

Following the usual rules of calculus, we would write

$$\begin{aligned} df &= f[x(t) + dx(t)] \\ &\quad - f[x(t)] \\ &= f' dx. \end{aligned}$$

taking  $(dx)^2 = 0$ .

**Itô identity:** However, if  $f(x(t))$  is a function of a stochastic variable with  $dx = adt + bdW$  then  $f$  satisfies the SDE:

$$\begin{aligned} df &= f[x(t) + dx(t)] \\ &\quad - f[x(t)] \\ &= (af' + \frac{1}{2}bf'')dt \\ &\quad + bf'dW. \end{aligned}$$


---

In Ref. (41, 50) we used Itô calculus to evaluate these correlation functions. From a practical point of view, the Itô calculus is a tool for manipulating stochastic processes that are closely related to Brownian motion and Itô's lemma allows us to easily perform noise-averaged interactions. For the model at hand, the covariance of  $N(s)$  and  $N(t)$  is given by

$$\begin{aligned}\text{Cov}[N(s), N(t)] &= \langle (N(s) - \langle N(s) \rangle)(N(t) - \langle N(t) \rangle) \rangle \\ &= \frac{\sigma^2}{2\Gamma} \left[ e^{-\Gamma|t-s|} - e^{-\Gamma(t+s)} \right] + \sigma_{N_0}^2 e^{-\Gamma(s+t)},\end{aligned}\quad 43.$$

with  $\sigma_{N_0}^2$  being the variance of  $N(0)$ . Similarly, the variance

$$\text{Var}[N(t)] = \left( \sigma_{N_0}^2 - \frac{\sigma^2}{2\Gamma} \right) e^{-2\Gamma t} + \frac{\sigma^2}{2\Gamma} \quad 44.$$

also depends upon the initial fluctuation in the background population. Mathematically, the Fourier transform of the kernel of the integral in Eq. 41 provides the spectral density of the noisy process. In fact, a trivial modification of the approach would be to replace the kernel in Eq. 41 with another kernel reflecting a more complex spectral density. The resulting expressions for the responses will be more complex indeed. However, Itô's lemma provides a tractable route for computing the necessary response functions.

### 3.4. Predictions from the stochastic model

Having established the mathematical model, let us briefly recapitulate some of its features. First, we started by assuming that the background population dynamics give rise to a stochastic process  $N(t)$  that enters into the Heisenberg equations of motion for the system operators. In particular, we assumed that  $N(t)$  corresponds to an overdamped Brownian oscillator and that at time  $t = 0$  there is a non-stationary population of background excitations. These two mathematical assumptions can be relaxed to some extent if one has a more detailed description of the spectral density of the background process and the initial background population. Secondly, we assume that averages over exponential terms can be evaluated using the cumulant expansion. What then follows are the mathematical consequences as expressed in terms of the spectral responses of the model.

**3.4.1. Linear response.** The linear response for optical excitation is given by

$$S^{(1)}(t) = \frac{i}{\hbar} \langle \hat{\mu}(t) [\hat{\mu}(0), \rho(-\infty)] \rangle, \quad 45.$$

where  $\hat{\mu}(t) = \mu(\hat{a}_0^\dagger(t) + \hat{a}_0(t))$  is the excitonic transition dipole operator and  $\rho(-\infty)$  is the initial density matrix. The absorption spectrum is obtained by Fourier transformation.

Averaging over the fluctuations generates terms involving cumulants of the background noise, which result in terms such as

$$\left\langle \exp \left[ i2\gamma_1 \int_0^t N(\tau) d\tau \right] \right\rangle \approx e^{i2\gamma_1 g_1(t) - 2\gamma_1^2 g_2(t)}, \quad 46.$$

where  $\langle \dots \rangle$  denotes averaging over noise. Note that the exciton interaction strength is  $2\gamma_1$  in Eq. 6. Here, the first cumulant  $g_1(t)$  gives rise to a characteristic frequency shift as the background population decays:

$$g_1(t) = \int_0^t \langle N(\tau) \rangle d\tau = \frac{N_0}{\Gamma} (1 - e^{-\Gamma t}), \quad 47.$$

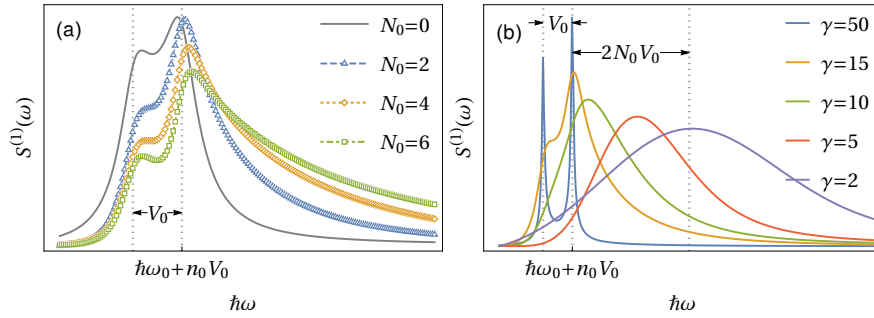


**Figure 9**

The linear response function with (a) increasing background population density  $N_0$ , and (b) different relaxation rate  $\Gamma$ , from the homogeneous limit of  $\Gamma = 50$  meV to the inhomogeneous limit of  $\Gamma = 2$  meV. (From Ref.50)

and

$$g_2(t, t') = \int_0^t \int_0^{t'} \text{Cov}[N(\tau), N(\tau')] d\tau' d\tau = \frac{\sigma^2}{2\Gamma^3} \left[ 2\Gamma \min(t, t') + 2e^{-\Gamma t} + 2e^{-\Gamma t'} - e^{-\Gamma|t'-t|} - e^{-\Gamma(t'+t)} - 2 \right] + \frac{\sigma_{N_0}^2}{\Gamma^2} \left[ e^{-\Gamma(t+t')} - e^{-\Gamma t} - e^{-\Gamma t'} + 1 \right]. \quad 48.$$

When the two time limits are the same, this reduces to

$$g_2(t) = \int_0^t \int_0^t \text{Cov}[N(\tau), N(\tau')] d\tau d\tau' = \frac{\sigma^2}{2\Gamma^3} (2\Gamma t + 4e^{-\Gamma t} - e^{-2\Gamma t} - 3) + \frac{\sigma_{N_0}^2}{\Gamma^2} (1 - e^{-\Gamma t})^2. \quad 49.$$

In Fig. 9 we highlight some of the key physical effects that can appear in the linear absorption spectra based upon our model. These effects are consistent with experimental observations and theoretical models of 2D semiconductors and transition metal dichalcogenides (27, 29, 38). Fig. 9(a) displays the effect of a non-stationary background on the linear absorption spectrum of a system. The notable feature is the tail that extends to higher absorption energies. The character of this tail depends most strongly upon the initial choice of  $N_0$  and is attributable to the  $g_1(t)$  term in our response function which is the time-integral over the evolving background population. This term, as it appears in Eq. 45, produces an *evolving* frequency shift reflecting the dynamical relaxation of the background. In the  $S^{(1)}$  response, the background evolution is manifest as a tail extending out to the blue.

#### Spectral effects that can be attributed to the non-stationary evolution.

1. **Blocking:** Increasing the initial background exciton density suppresses the peak absorption intensity.
2. **Biexciton formation:** The peak is split by  $\gamma_1/2$  corresponding biexciton interactions (38).
3. **(1D) Energy shift:** The peak position shifts to the blue with increasing background population due to increased Coulombic interactions.

4. **(1D) Broadening:** The spectrum acquires a long tail extending to the blue due to the dynamical evolution of the background.
5. **(2D) Phase scrambling:** appears in the 2D coherent spectroscopy as an asymmetry along the absorption axis and as phase scrambling in the rephasing and non-rephasing signals.
6. **(2D) Excitation-induced shift:** systematic shift of peak position that evolves as the background population decays.
7. **(2D) Excitation-induced dephasing:** Transient narrowing along the off-diagonal due to decreasing rate of exciton/exciton scattering.

Fig. 9(b) shows how the linear spectra is affected by the background relaxation rate  $\gamma$  for fixed values of  $N_0 = 4$ . In the case of fast background relaxation ( $\Gamma = 50\text{meV}$ ) the exciton and bi-exciton spitting is clearly resolved and the lineshapes are Lorentzian about each peak. Decreasing the relaxation rate  $\Gamma$  produces a systematic shift towards the blue due to the mean-field interaction between the exciton and the background population. This shift saturates when the peak is fully shifted by  $2V_0N_0$  and the spectral peak acquires a Gaussian form reflecting mean  $N_0$  and variance  $\sigma_{N_0}^2$  of the initial background. In this slow-relaxation limit, the “bright” state is simply swamped and suppressed by the background excitation.

**3.4.2. Two-dimensional coherent spectroscopy.** In Ref. 41 we discussed the linear response of our model and its relation to the Anderson-Kubo model. Here we shall focus solely on the higher-order responses that reveal the dynamic evolution of the two-dimensional coherent excitation line-shape. The third-order response involves phase-matched interactions of the system with a sequence of three laser pulses:

$$S^{(3)}(\tau_3, \tau_2, \tau_1) = \left(\frac{i}{\hbar}\right)^3 \langle \mu(\tau_3) [\mu(\tau_2), [\mu(\tau_1), [\mu(0), \rho(-\infty)]]] \rangle. \quad 50.$$

The times  $0 < \tau_1 < \tau_2 < \tau_3$  define the sequence of the time-ordered interactions in Fig. 10. The expressions for these can be evaluated using the standard rules for double-sided Feynman diagrams (Fig. 10, c.f. Ref. 44) representing various optical paths that for a given pathway take the form

$$R_\alpha(\tau_1, \tau_2, \tau_3) = \left(\frac{i}{\hbar}\right)^3 \mu^4(n_0 + 1)^2 \exp \left[ i(\omega_0 + n_0\gamma_1) \sum_{j=1}^3 (\pm)_j \tau_j \right] \left\langle \exp \left[ i2\gamma_1 \sum_{j=1}^3 (\pm)_j \int_0^{\tau_j} N(s) ds \right] \right\rangle \quad 51.$$

$$= \left(\frac{i}{\hbar}\right)^3 \mu^4(n_0 + 1)^2 \exp \left[ i(\omega_0 + n_0\gamma_1) \sum_{j=1}^3 (\pm)_j \tau_j \right] \times \exp \left[ i2\gamma_1 \sum_{j=1}^3 (\pm)_j g_1(\tau_j) \right] \exp \left[ -2\gamma_1^2 \sum_{i,j=1}^3 (\pm)_i (\pm)_j g_2(\tau_i, \tau_j) \right]. \quad 52.$$

The sign function  $(\pm)_j$  takes “+” and “−” depending upon whether or not the time-step involves an excitation or de-excitation of the system. The prefactor  $(n_0 + 1)^2$  is for the pathways involving only single excitation manifold (distinguished by subscript a), it is  $(n_0 + 1)(n_0 + 2)$  when double excitation (subscript b) is involved. Fig. 10 shows the most relevant diagrams for the rephasing and non-rephasing optical response.

It is important to notice that the exciton-exciton interaction term  $\gamma_1$ , and hence the screening due to exciton-lattice interactions, appears in three distinct places in the third-order responses. First,



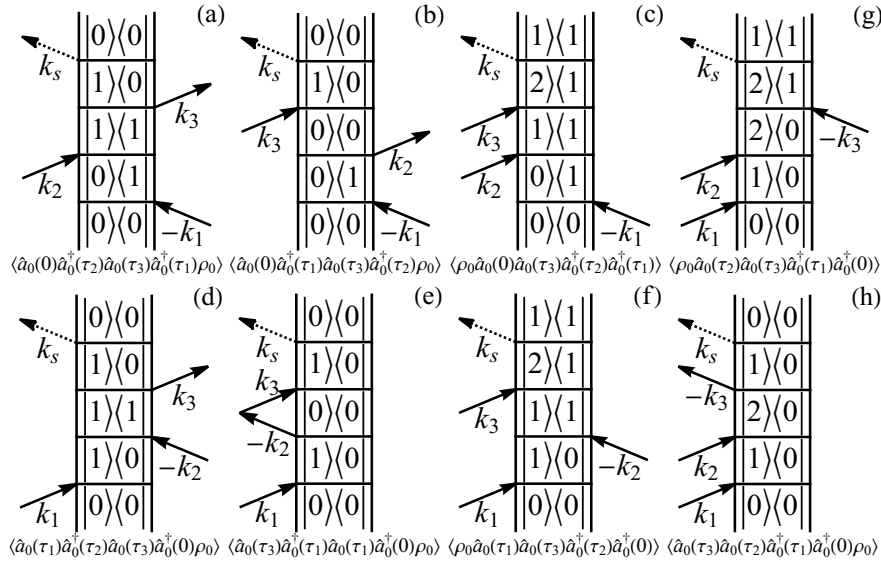


**Figure 10**

Double-sided Feynman Diagrams for coherent response functions (equation 52) with rephasing phase matching (top): (a)  $R_{2a}$ , (b)  $R_{3a}$ , (c)  $R_{1b}^*$ , non-rephasing phase matching (bottom): (d)  $R_{1a}$ , (e)  $R_{4a}$ , (f)  $R_{2b}^*$ , and double quantum phase matching: (g)  $R_{3b}^*$ , (h)  $R_{4b}$ .

as a frequency shift due to self-interactions between the bright excitons. Second, as a frequency shift due to interactions of bright excitons with the evolving background population density. Third, as the leading contribution to the lineshape. In addition, the third term involving  $g_2(t)$  carries the influence of the initial conditions (via  $\sigma_{N_0}$ ). The effect of many-body exciton-exciton scattering thus leads to time-evolving EID processes. Given these observations, we expect that the homogeneous linewidth will evolve with population time, dictated by the evolution of  $g_2(t)$ .

Figs. 11 and 12 correspond to the rephasing and non-rephasing behavior of theoretical model as parametrized to approximate the excitons in the 2D metal-halide perovskite system studied in the experimental investigations, which we shall describe later in this section. The parameters used to produce these spectra are given in Table 1. The two pairs of gray dashed lines correspond to the bare exciton energy at  $\hbar\omega_0 = 2.35$  eV and the dressed exciton energy at  $\hbar\omega_0 + \gamma_1 = 2.36$  eV. Fig. 11 gives the rephasing (a,b) and non-rephasing (c,d) spectra computed at  $\tau_p = 0$ . Two features highlighted above are immediately striking in the modelled 2D spectra. Both the asymmetry of the signals as well as the lineshape inversion of the real and imaginary spectral components can be traced specifically to terms within the response functions in Eq. 52 that depend upon the transient background relaxation and exciton self-interactions.

Both the phasing and asymmetry evolve with increasing population time as shown in Fig. 12(a-l). Importantly, the rephasing signal evolves being dispersive at  $\tau_p = 0$  to absorptive at longer times. The non-rephasing signal [Fig. 12(e-h)] has complementary behavior, evolving from absorptive to dispersive. Figs. 12(i-l) give the absolute value of the total response as it evolves over  $\tau_p$ . The peak is displaced from the diagonal and its position as well as the linewidth evolves over  $\tau_p$ .

In Fig. 12 we extract the contour corresponding to the half-maximum intensity at various indicated  $\tau_p$  population times. Superimposed over each contour is one of the principal axes of the contour scaled

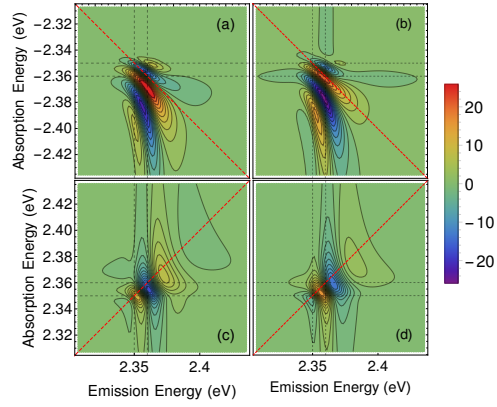


**Figure 11**

Theoretical real and imaginary spectra, respectively, of rephasing [(a), (b)] and nonrephasing [(c), (d)] phase matching and at population waiting time  $\tau_p = 0$  fs. The vertical false color scale indicated to the right of the figure is in arbitrary units.

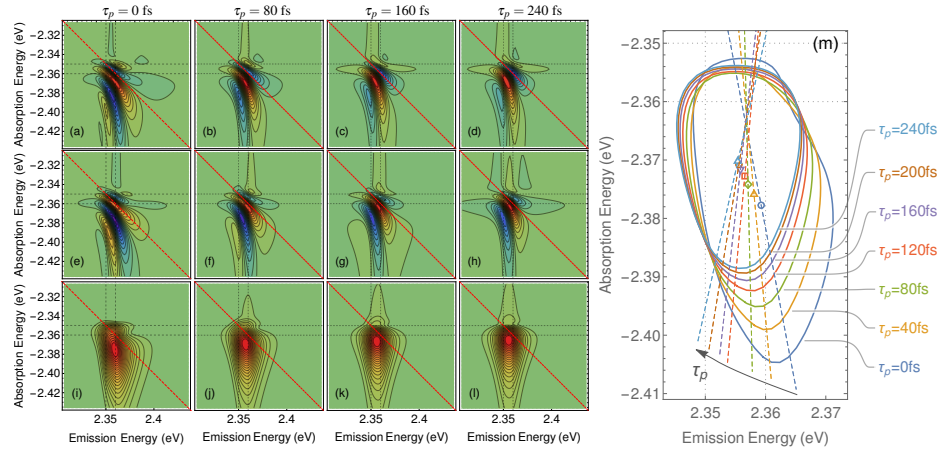


**Figure 12**

(a)–(d): Real parts of theoretical rephasing spectra at population times  $\tau_p$  indicated at the top of each panel. (e)–(h): Corresponding imaginary parts of the spectrum. (i)–(l): The norm (absolute value) of the optical response. Exciton 2D coherent lineshape contour at half-maximum intensity as a function of population waiting time derived from the theoretical rephasing absolute spectral evolution in Fig. 12. The center of mass and one of the principle axes are shown for each contour.

according to its magnitude. The central points are the geometric centers of contours. This analysis clearly shows that the peak systematically narrows, rotates, and distorts as the exciton co-evolves with the background population. Moreover, the center peak shifts by about 10 meV towards the red in both absorption and emission spectral dimensions as Coulombic interactions with the evolving background are diminished. (10).

Within the stochastic-model the frequency peak evolution is due to the first cumulant  $g_1(\pm\tau_1, \pm\tau_2, \pm\tau_3)$  which introduced a phase-shift that depends the background population evolution

as well as the background displacements following each interaction with the laser field. The early-time blue shift as well as more rapid dephasing arise from many-body effects contained within  $g_1$ . As the background population decays, the scattering effects are diminished. We note that in equation 52, if we set  $g_1 = 0$  the coherent response functions reduce to a stationary background, and the frequency peak evolution does not occur.

**Table 1** Parameters used in the theoretical model to produce Figs. 11 and 12.

Description	Symbol	Value
bare exciton energy	$\hbar\omega_0$	2.35 eV
noise variance	$\sigma^2$	0.0025 fs <sup>-1</sup>
relaxation rate	$\Gamma$	0.01 fs <sup>-1</sup>
exciton/exciton interaction	$\gamma_1$	10 meV
avg. init. background density	$N_0$	2 per unit volume
init. background variance	$\sigma_{N_0}$	0.35 per unit volume

We assume here that the initial background excitation is broad compared to its fluctuations about a stationary state and choose parameters to best represent the experimental conditions of an ultrafast experiment with  $\sim 20$  fs pulses.

### 3.5. Exciton/polaron formation dynamics due to exchange interactions

In deriving this model, we also assumed that an additional term corresponding to pair creation/annihilation could be dropped from consideration. That term takes the form

$$H_{pair} = \sum_{q \neq 0} \gamma_q (a_0^\dagger a_0^\dagger a_q a_{-q} + a_q^\dagger a_{-q}^\dagger a_0 a_0) \quad 53.$$

and corresponds to the Boson exchange interaction whereby momentum is transferred within the background population ( $q \neq 0$ ) as the result of interaction with the optical ( $q = 0$ ) exciton. However, such exchange terms may give important and interesting contributions to the spectral lineshape, especially in systems in which excitons are formed near the Fermi energy. In such systems, the exciton becomes dressed by virtual electron/hole fluctuations about the Fermi sea producing spectral shifts and broadening of the spectral lineshape. Such states are best described as exciton/polarons whose wave function consists of the bare exciton/hole excitation dressed by electron/hole fluctuations.

Ordinarily, as in the Bogoliubov treatment of Bose-Einstein condensates (51), one makes the semiclassical approximation that the condensate population can be taken as macroscopic and as a result, one can replace the  $a_0$  and  $a_0^\dagger$  operators with c-number  $\sqrt{N_0}$ . In our case, we shall continue to treat the background within the semiclassical limit and replace  $a_q$  and  $a_q^\dagger$  with  $\sqrt{N_q}$  and write the coupling

$$\gamma(t) = \sum_{q \neq 0} N_q \gamma_q \approx \gamma_{pair} N(t) \quad 54.$$

where  $\gamma_{pair}$  is the exchange coupling constant and  $N(t)$  the net background population at time  $t$ .

To pursue the effect of the exciton/polaron formation, we start with the basic form of the Hamiltonian

$$H = \hbar\omega_0(a^\dagger a + 1/2) + \hbar\gamma(t)(a^\dagger a^\dagger + aa)/2 \quad 55.$$

where  $\gamma(t)$  is the coupling which we take to be an unspecified stochastic process. One can bring  $H$  into a diagonal form by unitary transformation

$$\tilde{H} = e^{-S} H e^S = \hbar\tilde{\omega}_0(t) \left( \tilde{a}^\dagger \tilde{a} + 1/2 \right). \quad 56.$$

with

$$\tilde{\omega}_0(t) = \sqrt{\omega_0^2 - \gamma(t)^2}. \quad 57.$$

However, since  $\gamma(t)$  is a stochastic process, we need to use the Itô identity to properly derive the underlying SDE for the renormalized harmonic frequency,  $\tilde{\omega}_0(t)$ , in order to compute correlation functions.

In the regime of weak pair-excitation interaction,  $\gamma/\omega_0 \ll 1$ , the eigen-frequency can be approximated as

$$\begin{aligned} \tilde{\omega}_0(t) &= \omega_0 \sqrt{1 - (\gamma/\omega_0)^2} \\ &\approx \omega_0 (1 - z(t)/2), \end{aligned} \quad 58.$$

where  $z(t) = \gamma(t)^2/\omega_0^2$ . Therefore,  $\sqrt{z}$  represents the coupling strength of the pair-excitation relative to the excitation frequency. For the moment, we leave the stochastic variable unspecified and find the linear response function

$$\begin{aligned} S^{(1)}(t) &= \frac{i}{\hbar} \langle [\hat{\mu}(t), \hat{\mu}(0)] \rho(-\infty) \rangle \\ &= \frac{i}{\hbar} \mu^2 \langle [\hat{a}^\dagger(t), \hat{a}_0] \rho(-\infty) - \text{c.c.} \rangle \\ &= \frac{2\mu^2}{\hbar} \text{Im} \left\langle \exp(i\omega_0 t) \exp \left[ -\frac{i\omega_0}{2} \int_0^t z(\tau) d\tau \right] \right\rangle \end{aligned} \quad 59.$$

$$= \frac{2\mu^2}{\hbar} \text{Im} \left\{ \exp(i\omega_0 t) \exp \left[ \sum_{n=1}^{\infty} \frac{(-i\omega_0/2)^n}{n!} \left\langle \left( \int_0^t z(\tau) d\tau \right)^n \right\rangle_c \right] \right\} \quad 60.$$

in the form of cumulant expansion, where  $\langle x^n \rangle_c$  denotes the  $n$ -th cumulant. According to the theorem of Marcinkiewicz,(52, 53) the cumulant generating function is a polynomial of degree no greater than two to maintain the positive definiteness of the probability distribution function. Therefore, we truncate the cumulant expansion to the second order and write the spectral line-shape functions  $g_1(t)$  and  $g_2(t)$  from the first cumulant and second cumulants,

$$g_1(t) = \int_0^t \langle z(\tau) \rangle d\tau \quad 61.$$

and

$$g_2(t) = \int_0^t \int_0^t \langle z(\tau), z(\tau') \rangle d\tau d\tau', \quad 62.$$

respectively.

We now make the simplifying assumption that  $\gamma(t)$  satisfies the Ornstein-Uhlenbeck process, corresponding to vacuum fluctuations about bare exciton state.

$$d\gamma_t = -\theta \gamma_t dt + \sigma dW_t. \quad 63.$$

We should emphasize that this is not properly in the regime of quantum fluctuations since we have not enforced the bosonic commutation relation within the background in making the semi-classical *ansatz*. This is clearly an avenue for future exploration. Applying the Itô identity, we arrive at a SDE for the exciton frequency,

$$dz_t = 2\theta \left( \frac{\sigma^2}{2\theta\omega_0^2} - z_t \right) dt + \frac{2\sigma}{\omega_0} \sqrt{z_t} dW_t, \quad 64.$$

in which the relaxation rate is  $2\theta$ , and the drift term  $\sigma^2/2\theta\omega_0^2$  corresponds to the mean value of the stationary state. The formal solution, analogous to  $\gamma(t)$  as the solution of the Ornstein-Uhlenbeck SDE, is

$$\begin{aligned} z(t)^{1/2} &= [z(0)]^{1/2} e^{-\theta t} + \frac{\sigma}{\omega_0} \int_0^t e^{-\theta(t-s)} dW_s, \\ \gamma(t) &= \gamma(0) e^{-\theta t} + \sigma \int_0^t e^{-\theta(t-s)} dW_s. \end{aligned} \quad 65.$$

Using Itô isometry we find the mean value

$$\langle z(t) \rangle = z_0 e^{-2\theta t} + \frac{\sigma^2}{2\omega_0^2 \theta} (1 - e^{-2\theta t}), \quad 66.$$

and the correlation function

$$\langle z(t), z(s) \rangle = \sigma_{z_0}^2 e^{-2\theta(t+s)} + \frac{\sigma^4}{2\theta^2 \omega_0^4} [e^{-\theta|t-s|} - e^{-\theta(t+s)}]^2 + \frac{2\sigma^2}{\theta \omega_0^2} z_0 e^{-\theta(t+s)} [e^{-\theta|t-s|} - e^{-\theta(t+s)}], \quad 67.$$

which can be used to construct the  $g_1$  and  $g_2$  cumulants. Here the initial distribution of  $z$  is determined by the mean  $z_0 = \langle z(0) \rangle$ , and the variance  $\sigma_{z_0}^2 = \langle (z(0) - z_0)^2 \rangle$ .

$$\begin{aligned} g_1(t) &= \int_0^t \langle z(\tau) \rangle d\tau \\ &= \frac{\sigma^2 t}{2\theta \omega_0^2} + \frac{1}{2\theta} \left( z_0 - \frac{\sigma^2}{2\theta \omega_0^2} \right) (1 - e^{-2\theta t}), \end{aligned} \quad 68.$$

The first cumulant of the model produces a red shift that more complex than the counterpart in the simpler model where interactions between paired-excitations are neglected. The initial frequency shift  $z_0\omega_0/2$  agrees with the Anderson-Kubo theory, but converges to  $\sigma^2/4\theta\omega_0$  rather than decaying to zero. The first term then can be considered as a correction term that accounts for the interaction of exchange terms and leads to a constant red shift of  $\sigma^2/4\theta\omega_0$ .

#### Implications from the exciton/exciton exchange term

1. The model produces the lineshape function given by the Anderson-Kubo model in the stationary limit, albeit with twice the coherence time;
2. The model captures the formation of exciton/polarons as the steady-state/long-time limit and gives an exciton/polaron reorganization energy of  $\sigma^2/4\theta\omega_0$  that reflects the coupling and spectral density of the background.

The second cumulant,  $g_2(t)$ , evaluates to

$$\begin{aligned} g_2(t) &= \int_0^t \int_0^t \langle z(\tau), z(\tau') \rangle d\tau d\tau' \\ &= \frac{\sigma_{z_0}^2}{4\theta^2} (1 - e^{-2\theta t})^2 + \frac{\sigma^4}{8\theta^4 \omega_0^4} (e^{-4\theta t} + 8\theta t e^{-2\theta t} + 4e^{-2\theta t} + 4\theta t - 5) \\ &\quad + \frac{\sigma^2}{2\theta^3 \omega_0^2} z_0 (1 - 4\theta t e^{-2\theta t} - e^{-4\theta t}) \end{aligned} \quad 69.$$

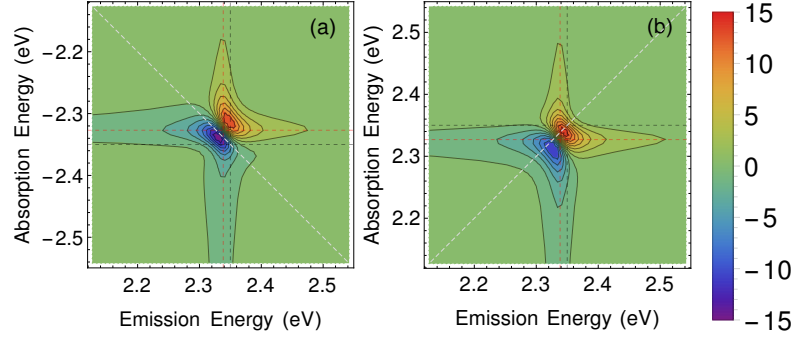


**Figure 13**

Real spectra of rephasing (a) and non-rephasing (b) signal computed by the exciton/polaron formation model.

If we compare this to the spectral function derived above

$$g_2^{\text{EID}}(t) = \frac{\sigma_{\gamma_0}^2}{\theta^2} \left(1 - e^{-\theta t}\right)^2 + \frac{\sigma^2}{2\theta^3} \left(2\theta t + 4e^{-\theta t} - e^{-2\theta t} - 3\right). \quad 70.$$

the first term is recovered; however, the present model provides a more sophisticated description of the dependency on the initial average  $z_0$ . In the limiting case of stationary state where  $\sigma_{\gamma_0}^2 = \sigma^2/2\theta$ , the second cumulant in the present model turns into

$$g_2(t) = \frac{\sigma^4}{4\theta^4\omega_0^4} \left(e^{-2\theta t} + 2\theta t - 1\right) + \frac{\sigma^2\gamma_0^2}{\theta^3\omega_0^4} (e^{2\theta t} - 2\theta t - 1)e^{-2\theta t}, \quad 71.$$

in which the first term reproduces the Anderson-Kubo lineshape but with half correlation time  $\tau_c = (2\theta)^{-1}$  compared to that of the Anderson-Kubo theory  $\theta^{-1}$ . Furthermore, the second term gives the line broadening due to the initial average of the background exciton population,  $\gamma_0^2$ , which only results in a frequency shift in our previous model.

**3.5.1. Effect on 2D spectroscopy.** The inhomogeneous and homogeneous contributions to the lineshape can be separated using 2D coherent spectroscopic methods. (35, 42, 43, 54, 55) In most molecular applications of 2D spectroscopy, the evolving background plays little to no role in the spectral dynamics. However, evolving background does affect the spectral lineshape by mixing absorptive and dispersive features in the real and imaginary spectral components. Generally speaking, systems lacking background dynamics exhibit absorptive line-shapes and dispersive lineshapes are a consequence of many-body correlations (41), consistent with the analysis of similar measurements in semiconductor quantum wells (22). Furthermore it is useful to compare the model presented here, which pertains to the exciton/exciton exchange coupling, versus our previous model which did not include this term and only considered the direct (Hartree) interaction. For this, we compute the third-order response  $S^{(3)}$  from Eq. 50 under the impulsive/rotating-wave approximation. One easily finds the responses for the various Liouville-space pathways take the form

$$R_\alpha(\tau_3, \tau_2, \tau_1) = \left(\frac{i}{\hbar}\right)^3 \mu^4 \left\langle \exp \left[ i \sum_{j=1}^3 (\pm)_j \int_0^{\tau_j} \tilde{\omega}_0(\tau) d\tau \right] \right\rangle \quad 72.$$

where the angular brackets denote averaging over the stochastic noise term and the  $(\pm)_j$  corresponds to whether or not the time-step involves an excitation (+) or de-excitation (-) of the system. The

time-ordering of the three optical pulses in the experiment and phase-matching conditions define the specific excitation pathways, based on which *photon echo* ( $k_s = -k_1 + k_2 + k_3$ ) and *virtual echo* ( $k_s = +k_1 - k_2 + k_3$ ) signals can be obtained by heterodyne detection (the fourth pulse) (43). Equivalently, in the experiments using co-linear phase-modulated pulses, *rephasing*  $[-(\phi_{43} - \phi_{21})]$  and *non-rephasing*  $[-(\phi_{43} + \phi_{21})]$  signals can be measured. In the rephasing experiment, the pulse sequence is such that the phase evolution of the polarization after the first pulse and the third pulse are of opposite sign, while in the non-rephasing experiment, they are of the same sign. Eq.(72) can be evaluated by cumulant expansion and the full expressions are given in the Appendix. Since the  $\tilde{\omega}_0(\tau)$  corresponds to a *non-stationary* process, both the lineshape functions  $g_1$  and  $g_2$  contribute to the output signal.

Fig. 14 presents the 2D rephasing and non-rephasing spectra corresponding to a single quantum state dressed by the pair-excitation terms. Focusing on the effect of interactions of paired excitations, rather than that of the initial condition, we set  $\sigma_{\gamma_0}^2 = \sigma^2/(2\theta)$  so that the initial fluctuation is the same as that of the Wiener process(50). The initial distribution of  $z(0)$  is given by that of  $\gamma(0)$

$$\omega_0^2 z_0 = \sigma_{\gamma_0}^2 + \gamma_0^2, \quad 73a.$$

$$\omega_0^4 \sigma_{z_0}^2 = 2\sigma_{\gamma_0}^4 + 4\sigma_{\gamma_0}^2 \gamma_0^2. \quad 73b.$$

The “dispersive” lineshape is observed in the real spectra for both rephasing and non-rephasing pulse sequences, which is a clear indication of the EID. The center of the peak deviates from the bare exciton energy  $\hbar\omega_0 = 2.35$  eV (black dashed lines) due to the coupling between exciton pairs. Both the absorption and emission energies shift to red because  $z(t)$  is positive by definition Eq.(58). Although the Hamiltonian is diagonal after the exciton/polaron transformation using matrix  $S$ , the diagonal peaks are off the diagonal. Noting Eqs.(58) and (66), we find that the emission frequency shift from  $\omega_0$  by  $-\sigma^2/(4\theta\omega_0)$  (red dashed line), as long as the time scale of the experiment is greater than the relaxation time  $(2\theta)^{-1}$ . Indeed, this energy discrepancy attributed to stationary state of  $z(t)$  can be considered as the exciton/polaron dressing energy. Regarding the absorption frequency measured by the first two pulses, because the system may not have sufficient time to relax, we can estimate, from Eq.(66), that the shift ranges between  $\omega_0 z_0/2$  and  $\sigma^2/(4\theta\omega_0)$ . The median  $\omega_0 z_0/4 + \sigma^2/(8\theta\omega_0)$  is shown as red dashed line for absorption.

**3.5.2. Comparison to the Anderson-Kubo model and our previous excitation-induced dephasing (EID) theory.** The well-known Anderson-Kubo theory describes the line shape broadening with regard to the stationary state of a random variable (usually the frequency fluctuation,  $z_t$  here) characterized by an Ornstein-Uhlenbeck process. The expansion of the linear optical response function leads to the first cumulant  $g_1^{\text{AK}}(t) = \beta t$ , in which  $\beta$  is the drift term, i.e., the long-term mean value, and the second cumulant

$$g_2^{\text{AK}}(t) = \frac{\sigma^2}{2\theta^3} (e^{-\theta t} + \theta t - 1). \quad 74.$$

In the short time limit  $\theta t \ll 1$ , the first cumulant in Eq. (68) turns to  $g_1(t) \approx z_0 t$ , which has the same linear form as  $g_1^{\text{AK}}(t)$ . It also agrees with our previous model in Section. 3.4.1 Eq. 47 (41, 50)

$$g_1^{\text{EID}}(t) = \frac{z_0}{2\theta} (1 - e^{-2\theta t}) \approx z_0 t. \quad 75.$$

It is worth noting that the relaxation rate here is  $2\theta$  instead of  $\theta$ , because  $\gamma(t)^2$  is the stochastic process of interest rather than  $\gamma(t)$  characterized by the rate  $\theta$ . For deterministic initial condition,  $z_0 = \gamma_0^2/\omega_0^2$ . The first cumulant  $g_1(t)$  results in a red shift of  $z_0\omega_0/2$  in the linear spectrum in the short time limit, which is determined by the initial average of the stochastic process  $z(t)$ .

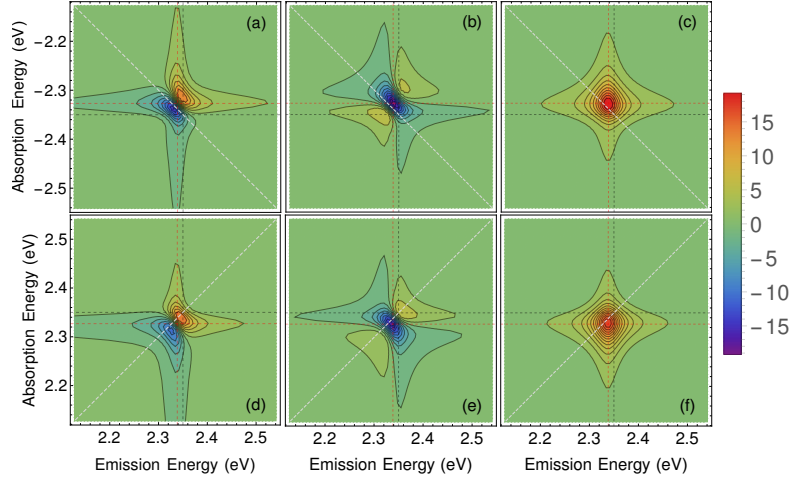


**Figure 14**

Rephasing (top) and non-rephasing (bottom) spectra at population time 100 fs based on the SDE in Eq.(63). (a) and (d) are the real, (b) and (e) are the imaginary, (c) and (f) are the norm of the spectra. The parameters used in the simulation:  $\hbar\omega_0 = 2.35$  eV,  $\sigma = 0.05$  fs<sup>-3/2</sup>,  $\theta = 0.01$  fs<sup>-1</sup>, and  $\gamma_0 = 0.5$  fs<sup>-1</sup>.

When the initial fluctuation of  $\gamma(t)$  obeys the same Ornstein-Uhlenbeck process, we conclude  $\sigma_{\gamma_0}^2 = \sigma^2/2\theta$  from the stationary state corresponding to the long-time limit where Eq. (66) turns into  $\text{Var}[\gamma(t)] = \sigma^2/2\theta$ . Considering Eq. (73a), we recast Eq. 68 into

$$g_1(t) = \frac{\sigma^2}{2\theta\omega_0^2}t + \frac{\gamma_0^2}{2\theta\omega_0^2} \left(1 - e^{-2\theta t}\right), \quad 76.$$

in which the second term looks similar to the  $g_1^{\text{EID}}(t)$  function in Eq. (75). However,  $z_0 = \gamma_0^2/\omega_0^2$  is true only for the deterministic initial condition, which is not the case in the above equation. Eq. (75) given in our previous model leads to a time-dependent red shift that eventually vanishes after sufficiently long time. The first term then can be considered as a correction term that accounts for the interaction of paired-excitation and leads to a constant red shift of  $\sigma^2/4\theta\omega_0$ .

Therefore, the first cumulant of the present model produces the red shift similar to but more complex than the counterpart in our previous model, where interactions between paired-excitations are neglected. The initial frequency shift  $z_0\omega_0/2$  agrees with the Anderson-Kubo theory, but converges to  $\sigma^2/4\theta\omega_0$  rather than decaying to zero as in the previous model.

Regarding the second cumulant,  $g_2(t)$ , Compared the result from the previous model Eq. 49 to Eq. 69, the second term is recovered; however, the present model provides a more sophisticated description of the dependency on the initial average  $z_0$ .

In the limiting case of stationary state where  $\sigma_{\gamma_0}^2 = \sigma^2/2\theta$ , the second cumulant in the present model turns into

$$g_2(t) = \frac{\sigma^4}{4\theta^4\omega_0^4} \left(e^{-2\theta t} + 2\theta t - 1\right) + \frac{\sigma^2\gamma_0^2}{\theta^3\omega_0^4} (e^{2\theta t} - 2\theta t - 1)e^{-2\theta t}, \quad 77.$$

in which the first term reproduces the Anderson-Kubo lineshape but with half correlation time  $\tau_c = (2\theta)^{-1}$  compared to that of the Anderson-Kubo theory  $\theta^{-1}$ . Furthermore, the second term gives the line broadening due to the initial average of the background exciton population,  $\gamma_0^2$ , which only results in a frequency shift in our previous model.



## 4. Perspective


Stochastic models have a long and important history in the field of chemical physics since they allow one to incorporate a trajectory-based viewpoint directly into the dynamics. The Anderson/Kubo model was an early attempt at providing a physical rationalization of how frequency fluctuations contribute to the absorption and emission lineshapes of molecules in contact with a thermal environment. (32, 33, 56) The models have been continuously improved upon over the years, notably including more detailed descriptions of the bath and the actual coupling mechanisms between the system and the environment that lead to the frequency fluctuations. (44, 57–60) As we have repeatedly pointed out, such approaches assume that the environment is in a stationary (e.g. thermal) state at time  $t = 0$  and does not interact with any external stimulus over the course of the dynamics of the system. We argue here, that in many cases one can not ignore the fact that the broad-band excitation pulses used in contemporary ultrafast experiments can create a background gas of excitons that can interact with an optical bright state—leading to fluency-dependent dynamics that can be manifest in terms of spectral shifts and tails even in linear absorption spectra. We conclude that these details can be further revealed through 2D coherent spectroscopy, especially when paired with a theoretical approach that accounts for the non-stationary evolution of the background.

Here we have reviewed our approach based upon a stochastic many-body treatment of the background and have provided a number of principal results and some technical details of our theoretical models. Throughout, we have used the Itô stochastic calculus approach when integrating over stochastic variables. This mathematical method provides us with a powerful avenue for obtaining analytical expressions for the various cumulants and correlation functions needed to compute the spectral responses. Fortunately, the current release of Mathematica ( $v > 10$ ) has a powerful stochastic calculus module that can be harnessed to evaluate both formally and numerically the cumulants and correlation functions for simple and complex transformed processes.

### Open questions

We conclude this review by posing a number of open questions that we are currently addressing:

1. Our current model assumes a mean-field/semiclassical treatment. Can this be extended to include correlations between the optical and non-optical degrees of freedom?
2. How does one include multiple bands or a more accurate description of the dark-state density of states?
3. Can a similar model be developed for fermionic degrees of freedom allowing separate treatment of electron and hole degrees of freedom?
4. Can the spectral response be “inverted” to reveal an underlying stochastic model for the background spectral density?
5. While the EID and EIS effects appear to be largely present in semiconductor systems and quantum dots, can similar effects be observed in molecular-based systems?
6. In ionic semiconductors such as the Ruddlesden-Popper metal halides described in this review, how do the EID quantum dynamics reflect the polaronic nature of excitons? What is the effect of metal, halide, and organic cation substitution on the homogeneous linewidth?
7. Can this approach be used to model the effects of dark-states present in microcavity polaritonic systems?
8. Can the model be extended towards the strongly quantum limit to model interacting quantum photons?



With regards to this last open question, we recently have demonstrated how frequency correlations between emitters can be detected using quantum photons. In particular, we show that pairs of photons, originating in a common Fock-state, can become entangled via interactions with quantum emitters that are correlated only through their interaction with a mutual environment. Our analysis indicates that the cross-correlation can be detected by observing the change in the entanglement entropy of scattered bi-photon states. (36, 61) This latter example is probably best taken as a thought experiment since an experimental realization of this will certainly be non-trivial due to contemporary difficulties in preparing and detecting high-quality bi-photon states at a sufficient flux to produce sufficient output signal. However, the theoretical results are highly tantalizing and we look forward to future developments along these lines.

## DISCLOSURE STATEMENT

The authors are not aware of any affiliations, memberships, funding, or financial holdings that might be perceived as affecting the objectivity of this review.

## ACKNOWLEDGMENTS

The work at the University of Houston was funded in part by the National Science Foundation (CHE-2102506) and the Robert A. Welch Foundation (E-1337). The work at LANL was funded by Laboratory Directed Research and Development (LDRD) program, 20220047DR. The work at Georgia Tech was funded by the National Science Foundation (DMR-1904293).

## LITERATURE CITED

1. Mysyrowicz A, Grun J, Levy R, Bivas A, Nikitine S. 1968. Excitonic molecule in CuCl. *Phys. Lett. A* 26(12):615–616
2. Magde D, Mahr H. 1970. Exciton-exciton interaction in CdS, CdSe, and ZnO. *Phys. Rev. Lett.* 24(16):890
3. Grun J, Nikitine S, Bivas A, Levy R. 1970. Luminescence of copper halides excited by a high power laser. *J. Lumin.* 1:241–253
4. Miller R, Kleinman D, Gossard A, Munteanu O. 1982. Biexcitons in GaAs quantum wells. *Phys. Rev. B* 25(10):6545
5. Kleinman D. 1983. Binding energy of biexcitons and bound excitons in quantum wells. *Phys. Rev. B* 28(2):871
6. Hu Y, Koch SW, Lindberg M, Peyghambarian N, Pollock E, Abraham FF. 1990. Biexcitons in semiconductor quantum dots. *Phys. Rev. Lett.* 64(15):1805
7. Brunner K, Abstreiter G, Böhm G, Tränkle G, Weimann G. 1994. Sharp-line photoluminescence and two-photon absorption of zero-dimensional biexcitons in a GaAs/AlGaAs structure. *Phys. Rev. Lett.* 73(8):1138
8. Albrecht T, Bott K, Meier T, Schulze A, Koch M, et al. 1996. Disorder mediated biexcitonic beats in semiconductor quantum wells. *Phys. Rev. B* 54(7):4436
9. Stone KW, Gundogdu K, Turner DB, Li X, Cundiff ST, Nelson KA. 2009. Two-quantum 2d ft electronic spectroscopy of biexcitons in GaAs quantum wells. *Science* 324(5931):1169–1173
10. Karauskaj D, Bristow AD, Yang L, Dai X, Mirin RP, et al. 2010. Two-quantum many-body coherences in two-dimensional Fourier-transform spectra of exciton resonances in semiconductor quantum wells. *Phys. Rev. Lett.* 104(11):117401
11. Turner DB, Nelson KA. 2010. Coherent measurements of high-order electronic correlations in quantum wells. *Nature* 466(7310):1089–1092
12. Schultheis L, Kuhl J, Honold A, Tu CW. 1986. Ultrafast phase relaxation of excitons via exciton-exciton and exciton-electron collisions. *Phys. Rev. Lett.* 57(13):1635–1638
13. Honold A, Schultheis L, Kuhl J, Tu CW. 1989. Collision broadening of two-dimensional excitons in a GaAs single quantum well. *Phys. Rev. B* 40(9):6442–6445
14. Wang H, Ferrio K, Steel DG, Hu YZ, Binder R, Koch SW. 1993. Transient nonlinear optical response from excitation induced dephasing in GaAs. *Phys. Rev. Lett.* 71(8):1261–1264
15. Wang H, Ferrio KB, Steel DG, Berman PR, Hu YZ, et al. 1994. Transient four-wave-mixing line shapes: Effects of excitation-induced dephasing. *Phys. Rev. A* 49(3):R1551–R1554
16. Hu YZ, Binder R, Koch SW, Cundiff ST, Wang H, Steel DG. 1994. Excitation and polarization effects in semiconductor four-wave-mixing spectroscopy. *Phys. Rev. B* 49(20):14382–14386
17. Rappen T, Peter UG, Wegener M, Schäfer W. 1994. Polarization dependence of dephasing processes: A probe for many-body effects. *Phys. Rev. B* 49(15):10774–10777
18. Wagner HP, Schätz A, Maier R, Langbein W, Hvam JM. 1997. Coherent optical nonlinearities and phase relaxation of quasi-three-dimensional and quasi-two-dimensional excitons in  $\text{ZnS}_x\text{Se}_{1-x}/\text{ZnSe}$  structures. *Phys. Rev. B* 56(19):12581–12588

19. Wagner HP, Schätz A, Langbein W, Hvam JM, Smirl AL. 1999. Interaction-induced effects in the nonlinear coherent response of quantum-well excitons. *Phys. Rev. B* 60(7):4454–4457
20. Shacklette JM, Cundiff ST. 2002. Role of excitation-induced shift in the coherent optical response of semiconductors. *Phys. Rev. B* 66(4):045309
21. Shacklette JM, Cundiff ST. 2003. Nonperturbative transient four-wave-mixing line shapes due to excitation-induced shift and excitation-induced dephasing. *J. Opt. Soc. Am. B* 20(4):764–769
22. Li X, Zhang T, Borca CN, Cundiff ST. 2006. Many-body interactions in semiconductors probed by optical two-dimensional fourier transform spectroscopy. *Phys. Rev. Lett.* 96(5):057406
23. Moody G, Siemens ME, Bristow AD, Dai X, Karauskaj D, et al. 2011. Exciton-exciton and exciton-phonon interactions in an interfacial GaAs quantum dot ensemble. *Phys. Rev. B* 83(11):115324
24. Nardin G, Moody G, Singh R, Autry TM, Li H, et al. 2014. Coherent excitonic coupling in an asymmetric double ingaas quantum well arises from many-body effects. *Phys. Rev. Lett.* 112(4):046402
25. Moody G, Dass CK, Hao K, Chen CH, Li LJ, et al. 2015. Intrinsic homogeneous linewidth and broadening mechanisms of excitons in monolayer transition metal dichalcogenides. *Nat. Commun.* 6:8315
26. Martin EW, Horng J, Ruth HG, Paik E, Wentzel MH, et al. 2018. Encapsulation narrows excitonic homogeneous linewidth of exfoliated MoSe<sub>2</sub> monolayer. arXiv:1810.09834 [cond-mat.mtrl-sci]
27. Thouin F, Cortecchia D, Petrozza A, Srimath Kandada AR, Silva C. 2019. Enhanced screening and spectral diversity in many-body elastic scattering of excitons in two-dimensional hybrid metal-halide perovskites. *Phys. Rev. Res.* 1:032032
28. Karki KJ, Widom JR, Seibt J, Moody I, Loneragan MC, et al. 2014. Coherent two-dimensional photocurrent spectroscopy in a pbs quantum dot photocell. *Nature Communications* 5(1):5869
29. Katsch F, Selig M, Knorr A. 2020. Exciton-scattering-induced dephasing in two-dimensional semiconductors. *Phys. Rev. Lett.* 124(25):257402
30. Erkensten D, Brem S, Malic E. 2020. Excitation-induced dephasing in 2D materials and van der Waals heterostructures. arXiv:2006.08392 [cond-mat.mtrl-sci]
31. Srimath Kandada AR, Silva C. 2020. Exciton polarons in two-dimensional hybrid metal-halide perovskites. *J. Phys. Chem. Lett.* 11(9):3173–3184
32. W. Anderson P. 1954. A mathematical model for the narrowing of spectral lines by exchange or motion. *Journal of the Physical Society of Japan* 9(3):316–339
33. Kubo R. 1954. Note on the stochastic theory of resonance absorption. *Journal of the Physical Society of Japan* 9(6):935–944
34. Siemens ME, Moody G, Li H, Bristow AD, Cundiff ST. 2010. Resonance lineshapes in two-dimensional Fourier transform spectroscopy. *Optics Express* 18(17):17699–17708
35. Bristow AD, Zhang T, Siemens ME, Cundiff ST, Mirin R. 2011. Separating homogeneous and inhomogeneous line widths of heavy-and light-hole excitons in weakly disordered semiconductor quantum wells. *J. Phys. Chem. B* 115(18):5365–5371
36. Li H, Piryatinski A, Srimath Kandada AR, Silva C, Bittner ER. 2019. Photon entanglement entropy as a probe of many-body correlations and fluctuations. *The Journal of Chemical Physics* 150(18):184106
37. Neutzner S, Thouin F, Cortecchia D, Petrozza A, Silva C, Srimath Kandada AR. 2018. Exciton-polaron spectral structures in two dimensional hybrid lead-halide perovskites. *Phys. Rev. Mater.* 2(6):064605
38. Thouin F, Neutzner S, Cortecchia D, Dragomir VA, Soci C, et al. 2018. Stable biexcitons in two-dimensional metal-halide perovskites with strong dynamic lattice disorder. *Phys. Rev. Mater.* 2(3):034001
39. Thouin F, Valverde-Chávez DA, Quarti C, Cortecchia D, Bargigia I, et al. 2019. Phonon coherences reveal the polaronic character of excitons in two-dimensional lead halide perovskites. *Nat. Mater.* 18:349–356
40. Thouin F, Srimath Kandada AR, Valverde-Chávez DA, Cortecchia D, Bargigia I, et al. 2019. Electron-phonon couplings inherent in polarons drive exciton dynamics in two-dimensional metal-halide perovskites. *Chem. Mater.* 31:7085–7091
41. Srimath Kandada AR, Li H, Thouin F, Bittner ER, Silva C. 2020. Stochastic scattering theory for excitation-induced dephasing: Time-dependent nonlinear coherent exciton lineshapes. *The Journal of Chemical Physics* 153(16):164706
42. Srimath Kandada AR, Li H, Bittner ER, Silva-Acuña C. 2022. Homogeneous optical line widths in hybrid

- ruddlesden–popper metal halides can only be measured using nonlinear spectroscopy. *The Journal of Physical Chemistry C* 126(12):5378–5387
43. Cho M. 2008. Coherent two-dimensional optical spectroscopy. *Chem. Rev.* 108(4):1331–1418
  44. Mukamel S. 1995. *Principles of Nonlinear Optics and Spectroscopy*. Oxford University Press
  45. Ciuti C, Savona V, Piermarocchi C, Quattropani A, Schwendimann P. 1998. Role of the exchange of carriers in elastic exciton-exciton scattering in quantum wells. *Physical Review B* 58(12):7926–7933
  46. You Y, Zhang XX, Berkelbach TC, Hybertsen MS, Reichman DR, Heinz TF. 2015. Observation of biexcitons in monolayer WSe<sub>2</sub>. *Nature Physics* 11:477–482
  47. Kylänpää I, Komsa HP. 2015. Binding energies of exciton complexes in transition metal dichalcogenide monolayers and effect of dielectric environment. *Physical Review B* 92(20):205418
  48. Bolzonello L, Fassioli F, Collini E. 2016. Correlated fluctuations and intraband dynamics of j-aggregates revealed by combination of 2des schemes. *The Journal of Physical Chemistry Letters* 7(24):4996–5001 PMID: 27973862
  49. Born M. 1926. Quantenmechanik der stoßvorgänge. *Zeitschrift für Physik* 38(11-12):803–827
  50. Li H, Srimath Kandada AR, Silva C, Bittner ER. 2020. Stochastic scattering theory for excitation-induced dephasing: Comparison to the anderson–kubo lineshape. *The Journal of Chemical Physics* 153(15):154115
  51. de Gennes PG. 1999. *Superconductivity Of Metals And Alloys*. CRC PRes
  52. Marcinkiewicz J. 1939. Sur une propriété de la loi de Gauß. *Mathematische Zeitschrift* 44(1):612–618
  53. Rajagopal AK, Sudarshan ECG. 1974. Some generalizations of the marcinkiewicz theorem and its implications to certain approximation schemes in many-particle physics. *Phys. Rev. A* 10(5):1852–1857
  54. Fuller FD, Ogilvie JP. 2015. Experimental implementations of two-dimensional fourier transform electronic spectroscopy. *Annu. Rev. Phys. Chem.* 66:667–690
  55. Tokmakoff A. 2000. Two-dimensional line shapes derived from coherent third-order nonlinear spectroscopy. *J. Phys. Chem. A* 104(18):4247–4255
  56. Kubo R. 1969. A stochastic theory of line shape. John Wiley & Sons, Ltd, 101–127
  57. Reichman D, Silbey RJ, Suárez A. 1996. On the nonperturbative theory of pure dephasing in condensed phases at low temperatures. *The Journal of Chemical Physics* 105(23):10500–10506
  58. Hsu D, Skinner JL. 1984. On the thermal broadening of zero-phonon impurity lines in absorption and fluorescence spectra. *The Journal of Chemical Physics* 81(4):1604–1613
  59. Skinner JL, Hsu D. 1986. Pure dephasing of a two-level system. *The Journal of Physical Chemistry* 90(21):4931–4938
  60. Mukamel S. 1984. Stochastic theory of resonance Raman line shapes of polyatomic molecules in condensed phases. *The Journal of Chemical Physics*
  61. Bittner ER, Li H, Piryatinski A, Srimath Kandada AR, Silva C. 2020. Probing exciton/exciton interactions with entangled photons: Theory. *The Journal of Chemical Physics* 152(7):071101